

1 **Toward a versatile spaceborne architecture for immediate**
2 **monitoring of the global methane pledge**

3 Yuchen Wang¹, Xvli Guo¹, Yajie Huo¹, Mengying Li², Yuqing Pan^{1*}, Shaocai Yu^{2*}, Alexander
4 Baklanov³, Daniel Rosenfeld⁴, John H. Seinfeld⁵, and Pengfei Li^{1*}

5

6 ¹College of Science and Technology, Hebei Agricultural University, Baoding, Hebei 071000, P.R. China

7 ²Research Center for Air Pollution and Health; Key Laboratory of Environmental Remediation and Ecological Health,
8 Ministry of Education, College of Environment and Resource Sciences, Zhejiang University, Hangzhou, Zhejiang 310058,
9 P.R. China

10 ³Science and Innovation Department, World Meteorological Organization (WMO), Geneva, Switzerland

11 ⁴Institute of Earth Science, The Hebrew University of Jerusalem, Jerusalem, Israel

12 ⁵Division of Chemistry and Chemical Engineering, California Institute of Technology, Pasadena, CA 91125, USA

13

14 **Correspondence to:* Pengfei Li (lpf_zju@163.com)

15 Shaocai Yu (shaocaiyu@zju.edu.cn)

16 Yuqing Pan (panyuqing@hebau.edu.cn)

17

18

19

20

21

22

23

24

25

26

27

28

29 *Submitted to*

30 ***Atmospheric Chemistry and Physics***

31 **Abstract.**

32 The global methane pledge paves a fresh, critical way toward Carbon Neutrality. However, it remains largely invisible and
33 highly controversial due to the fact that planet-scale and plant-level methane retrievals have rarely been coordinated. This has
34 never been more essential within the narrow window to reach the Paris target. Here we present a two-tiered spaceborne
35 architecture to address this issue. Using this framework, we focused on the United States, China, the Middle East, and North
36 Africa, and simultaneously uncovered methane-abundant regions and plumes. These include new super-emitters, potential
37 leakages, and unprecedented multiple plumes in a single source. More importantly, this framework is shown to challenge
38 official emission reports that possibly mislead estimates from global, regional, to site scales, particularly by missing super-
39 emitters. Our results show that, in principle, the above framework can be extended to be multi-tiered by adding upcoming
40 stereoscopic measurements and suitable artificial intelligence, and thus is sufficiently versatile for immediate and future
41 monitoring of the global methane pledge.

42 **1. Introduction**

43 Global methane pledges finalized at the COP26 (the 26th United Nations Climate Change Conference of the Parties) have
44 been never more ambitious (Schellnhuber et al., 2016; Schurer et al., 2018; United Nations, 2021). More than 100 countries
45 have promised 30% methane emission reductions by 2030. Also, energy giants (e.g., Shell and BP) have committed to clear
46 targets of methane mitigation. Such pledges have never been more essential within the narrow window (< ten years) to reach
47 the Paris target. The scientific context is that atmospheric methane is a powerful greenhouse gas second only to carbon dioxide
48 (CO_2), trapping ~ 80 times more heat than the same amount of CO_2 (per molecule) over a 20-year time horizon (Etminan et
49 al., 2016; Saunois et al., 2016, 2020). Worse still, it has been rising since 2007 (Mikaloff and Hinrich, 2019), with a surge in
50 2014 (Nisbet et al., 2019) and a record high in 2021 (National Oceanic and Atmospheric Administration, 2022). Fortunately,
51 methane is short-lived (\sim ten years) (Shoemaker et al., 2013), and, particularly, that from human activities can be reduced in
52 half using existing technologies by 2030 (Ocko et al., 2021).

53 However, a classic dilemma emerges, dimming the hopes of scientists and policymakers (Masood and Tollefson, 2021). That
54 is, on the eve of the Paris target, large uncertainties in emissions remain, and thus hinder effective mitigation. The main issue
55 is the Paris framework relies on countries or corporate giants to report emissions (Allen et al., 2015; Alvarez, 2018; Ganesan
56 et al., 2019). Moreover, the reports are based on indirect statistics, such as O&G inventories, rather than direct measurements
57 (Deng et al., 2022). This leads to a broad consensus that prominent discrepancies exist between the reports. For example, field
58 campaigns report nearly double official claims of methane emissions in the United States by detecting leak detection (Alvarez,
59 2018).

60 To this end, widespread super-emitters present a unique opportunity worldwide (Duren et al., 2019; Lauvaux et al., 2022;
61 Pandey et al., 2019; Zavala-Araiza et al., 2015, 2017). Super-emitters can generally be defined as emission sources that
62 comprise highly concentrated methane plumes and dominate localized methane budgets ($\sim 5 \times 5 \text{ km}^2$). In contrast to region-
63 scale hotspots (or area sources), they can be attributed to individual facilities (e.g., factories, chimneys, and pipelines), typically
64 with dimensions varying from several meters to tens of meters depending on monitoring instruments. Super-emitters are
65 typically responsible for the underestimates of methane emissions (Alvarez et al., 2018; Duren et al., 2019; Irakulis-Loitxate
66 et al., 2021; Lauvaux et al., 2022; Thompson et al., 2016). Moreover, there is increasing evidence that methane emissions
67 follow a heavy-tailed distribution (Duren et al., 2019; Frankenberg et al., 2016; Lauvaux et al., 2022), for which relatively
68 small number of sources (so-called super-emitters) can account for a disproportionately large share of total emissions. In
69 contrast to area sources (e.g., cities), super-emitters are typically coal mines, wells, gathering stations, storage tanks, pipelines,
70 and flares, with diameters on the order of dozens of metres or less, but generating plumes of high-concentrated methane (Allen
71 et al., 2013; Miller et al., 2019; Subramanian et al., 2015; Varon et al., 2019). We thus anticipate that significant emission
72 mitigation could be achieved by deploying well-designed systems to identify methane super-emitters. For instance, in support
73 of the Paris agreement, the 17th World Meteorological Congress (2015) requested an Integrated Global Greenhouse Gas

74 Information System (IG3IS) that aimed to develop a measurement framework for methane emission reductions (Phil DeCola
75 and WMO Secretariat, 2017).

76 To date, a large body of field measurements (e.g., in situ and aircraft surveys) between 2012 and 2020 has been designed for
77 methane super-emitters. Despite this, they are spatially limited (e.g., regionally) and temporally infrequent (e.g., a few weeks),
78 missing many methane super-emitters (Alvarez, 2018; Conley et al., 2016; Duren et al., 2019; Marchese et al., 2015; Nisbet et
79 al., 2020; Smith et al., 2017; Thompson et al., 2016; Thorpe et al., 2016). Today, substantial advances have been made towards
80 detecting and quantifying methane super-emitters from space (Cusworth et al., 2019; Hu et al., 2018; Irakulis-Loitxate et al.,
81 2022; Jacob et al., 2016; Pandey et al., 2019; Thompson et al., 2016) (Table 1). Such advances, however, have rarely been
82 expanded to measure the global methane pledge because wide swaths and high-resolution sampling have not been
83 simultaneously available. Recently, global methane monitoring has become possible. A flagship satellite mission is the
84 TROPOspheric Monitoring Instrument (TROPOMI) onboard the Copernicus Sentinel-5 Precursor satellite (Lauvaux et al.,
85 2022; Veefkind et al., 2012). It provides daily global methane columns, with a large swath width of \sim 2600 km, a moderate
86 resolution of $7.0 \times 5.5 \text{ km}^2$ (since August 2019), and a high signal-to-noise ratio. However, its relatively coarse spatial sampling
87 still limits its application to detect methane super-emitters (Lauvaux et al., 2022). Next-generation satellite missions, pioneered
88 by the GHGSat constellation (three satellites at the moment), have emerged for mapping methane super-emitters (Cusworth et
89 al., 2019), with a narrow swath (e.g., \sim 12 km) but a ground-breaking high-resolution spatial sampling (e.g., 25 \sim 50 m) (Jervis
90 et al., 2021; Varon et al., 2020). Complementary to the GHGSat constellation, satellite-based hyperspectral imager
91 spectrometers, such as PRISMA, GF-5, ZY1, Sentinel-2, and Worldview-3, have shown great potential (Guanter et al., 2021;
92 Irakulis-Loitxate et al., 2021; Sánchez-García et al., 2021; Varon et al., 2021). They can resolve methane enhancements and
93 attribute them to specific infrastructures via similar narrow swath and high-resolution sampling (e.g., 30 m). Note that the
94 regions these satellites usually observed are already known to contain methane super-emitters. Narrow swath coverage thus
95 remains a crucial limitation for global surveys of methane super-emitters. Collectively, existing studies still struggle to survey
96 global methane super-emitters due to the fact that individual satellite missions, such as TROPOMI or PRISMA, do not both
97 have a wide swath and high resolution sampling.

98 To address this issue, we present a two-tiered, space-based framework that coordinates TROPOMI and PRISMA for both
99 planet-scale and plant-level methane retrievals. The key is that ready-made satellite missions alone have the potential to initiate
100 immediate monitoring of the global methane pledge. Using this framework, we focused on China, the United States, Iraq,
101 Kuwait, and Algeria, and reveal both region-scale hotspots and plant-level super-emitters. We also monitored a single source
102 to map multiple plumes and to look for possible methane leaks. These results can challenge national reports that possibly miss
103 unexpected super-emitters or mislead emission magnitude. On the eve of the Paris target, at least while a global methane
104 monitoring network is not in place, the two-tiered satellite constellation presented in this study has great potential for measuring
105 progress towards global methane pledges.

106 **2. Materials and Methods**

107 **2.1 Two-tiered satellite constellation**

108 The two-tiered satellite constellation is designed to reconcile global-scale and high-resolution methane monitoring. First,
109 TROPOMI offers a unique potential for global methane monitoring due to its large swath (i.e., ~ 2600 km), daily revisit time,
110 moderate footprint (i.e., 5.5×7 km 2 since August 2019), and excellent sounding precision and accuracy (i.e., $< 1\%$) (Veefkind
111 et al., 2012). TROPOMI observes approximately a full swath per second, resulting in ~ 216 spectra per second. This instrument
112 comprises two spectrometer modules, the first consisting of near-infrared (NIR) spectral channels, and the second dedicated
113 to the shortwave-infrared (SWIR) spectral channel. The NIR and SWIR channels are equipped with spectral resolutions of
114 0.38 and 0.25 nm and spectral sampling ratios of 2.8 and 2.5, respectively. Since the NIR and SWIR detectors are incorporated
115 in different instrument modules, the NIR spectra will be co-registered with the SWIR spectra before performing methane
116 retrievals. The methane total column-averaged dry-air mole fraction (XCH₄) is retrieved from near-infrared (NIR) (757 \sim 774
117 nm) and shortwave-infrared (SWIR) (2305 \sim 2385 nm) spectral measurements for sunlight backscattered by Earth's surface
118 and atmosphere (Hu et al., 2018). In this study, only high-quality measurements, retrieved under cloud-free and low aerosol
119 load conditions, are used. These measurements are filtered, in addition, for solar zenith angle ($< 70^\circ$), low viewing zenith angle
120 ($< 60^\circ$), and smooth topography (the surface elevation of < 80 m within 5 km radius) as described in Hu et al. (28) (Hu et al.,
121 2018).

122 Hyperspectral satellite missions serve as the second tier, responsible for mapping localized methane super-emitters due to their
123 unprecedented resolution (i.e., 3m \sim 50m). Therein PRISMA, as an open-access representative, is specifically suitable for this
124 work. It can image the solar radiation reflected by the Earth's surface and atmosphere via hundreds of spectral channels
125 between the visible and SWIR spectrum ($\sim 400 \sim 2500$ nm). Measurements in the SWIR spectrum from 2000 to 2500 nm
126 sample absorption features from water vapor, carbon dioxide, and methane. Therein the 2100 nm and 2450 nm windows are
127 especially sensitive to methane. Furthermore, the signal-to-noise ratio is reported to be about 100 in the SWIR for a relatively
128 dark vegetation pixel and increases up to above 200 for bright soil surfaces in oil and gas extraction sites. More importantly,
129 it covers areas of 30×30 km 2 with a 30 m spatial sampling.

130 We collect dozens of daily measurements from the two-tiered satellite constellation. These measurements experimentally map
131 regional methane hotspots and localize methane super-emitters across the United States, China, the Middle East (Iraq and
132 Kuwait), and North Africa (Algeria). The acquisitions are mostly taken between April 2020 and January 2022.

133 **2.2 Two-tiered methane retrievals**

134 In the first tier of our framework, we employ the operational TROPOMI methane products onboard the Sentinel 5 satellite.
135 The target product is the column-averaged dry-air volume mixing ratio of methane (XCH₄), which is retrieved simultaneously
136 with scattering properties of the atmosphere. The operational retrieval algorithm is based on RemoTeC (Butz et al., 2009;
137 Hasekamp and Butz, 2008), which is originally developed for CO₂ and methane retrievals from GOSAT observations (Butz et

138 al., 2011). It attempts to fit spectra observed by the TROPOMI-based NIR and SWIR channels. Its sensitivities to atmospheric
139 scattering properties, atmospheric input data, and instrument calibration errors have been extensively evaluated (Sha et al.,
140 2021; Verhoelst et al., 2021). As a result, the operational products are proved to be critically stable, with a convergence rate
141 of 99% and high significance as compared with both satellite-based (e.g., GOSAT) and ground-based (e.g., TCCON)
142 measurements. The required accuracy and precision of < 1 % for the XCH₄ product are met for clear-sky measurements over
143 land surfaces and after appropriate filtering of difficult scenes. Moreover, the forward model error is less than 1 % for about
144 95 % of the valid retrievals. Model errors in the input profile of water do not influence the retrieval outcome noticeably. The
145 methane product is expected to meet the requirements if errors in input profiles of pressure and temperature remain below 0.3%
146 and 2 K, respectively. Of all instrument calibration errors, the retrieval results are the most sensitive to an error in the instrument
147 spectral response function of the shortwave infrared channel.

148 In the second tier of our framework, we apply the matched-filter algorithm to calculate per-pixel methane enhancements with
149 respect to background levels based on the SWIR sample spectrum (i.e., the 2100 - 2450 nm window) onboard the PRISMA
150 (Foote et al., 2020; Guanter et al., 2021; Irakulis-Loitxate et al., 2021). In theory, the retrieval method can depend on
151 physically-based or data-driven algorithms. The former aims to explicitly resolve the radiative transfer between the surface,
152 the atmosphere, and the hyperspectral spectrometers. A key representative is the family of differential optical absorption
153 spectroscopy (DOAS) methods (Cusworth et al., 2019, 2020, 2021b, 2021a). The latter seeks a methane absorption spectrum
154 across a hyperspectral image using statistical methods. It is commonly based on the matched-filter and the singular vector
155 decomposition concepts. These methods are both widely applied and evaluated, especially for observations from instruments
156 deployed on satellite (e.g., PRISMA, GF-5, and ZY-1) and airborne (e.g., AVIRIS and AVIRIS-NG) platforms (Cusworth et
157 al., 2020; Foote et al., 2020; Guanter et al., 2021; Irakulis-Loitxate et al., 2021; Thompson et al., 2016; Thorpe et al., 2016).
158 In this study, the data-driven retrieval based on the matched-filter concept is used. The main reason is that it can implicitly
159 account for potential radiometric and spectral errors in satellite-based imaging spectroscopy. For instance, vertical striping is
160 prevalent in hyperspectral measurements due to detector inhomogeneity, thus substantially degrading methane retrievals. The
161 matched-filter algorithm focuses on the individual columns rather than the whole scene to resolve methane enhancements.
162 This means that the methane enhancement per column is calculated separately (i.e., methane enhancements were calculated
163 on a per-column basis). More explanations can be found in Guanter et al. (2021). Besides, the physically-based method requires
164 background concentrations that are difficult to determine around the super-emitters. In contrast, the data-driven method is
165 independent of background levels and can directly seek methane enhancements. Finally, the data-driven method generally has
166 a substantially superior computational efficiency compared to the physically-based method.

167 The matched-filter retrieval used here is similar to the one used by Thompson et al. (2016) for the Hyperion imaging
168 spectrometer onboard the EO-1 satellite. The calculation process of methane enhancements (**ΔXCH₄, ppb**) is as follows.

$$169 \Delta XCH_4(\vec{x}) = \frac{(\vec{x} - \vec{\mu})^T \Sigma^{-1} \vec{t}}{\vec{t}^T \Sigma^{-1} \vec{t}} \text{ (Eq. 1).}$$

170 The \vec{x} denotes the spectrum under analysis. The $\vec{\mu}$ and Σ represent the mean background radiance and corresponding
171 covariance, respectively. The $\vec{\mu}$ and Σ represent the mean value and covariance of the background radiance, respectively. To
172 avoid any contamination of the target spectrum into these background parameters, we estimate them with an iterative approach
173 by removing all gas enhancement signals. More technical details are reported in previous studies (Foote et al., 2020). Note
174 that, owing to the non-uniform response of individual detectors in PRISMA, enhancements are calculated based on per-column
175 spectrums in order to consider different responses of across-track sensors to radiance. The \vec{t} is the target spectrum that reflects
176 the background radiance enhanced by the methane plume. It is generated by the elementwise multiplication of $\vec{\mu}$ and \vec{k} . This
177 implicit parameter \vec{k} represents a unit methane absorption spectrum derived from a look-up table simulated by the MODTRAN
178 radiative transfer model. Similarly, the spectral convolution is also performed on a per-column basis.

179 In principle, it would be more difficult to detect methane enhancements in pixels over low-albedo surfaces. Although methane
180 absorption is independent of albedo, the resulting signal in absolute radiance is weakened with decreasing surface albedo. A
181 major measure to compensate for the albedo effect is to scale the target spectrum \vec{t} by the pixel-specific albedo factor due to
182 the fact that the Beer–Lambert absorption law depends on the initial radiance in the absence of the absorber. Here the pixel-
183 specific scalar f is calculated based on the spectral average $\vec{\mu}$ and the analysis spectrum \vec{x} as follows:

184
$$f = \frac{\vec{x}^T \vec{\mu}}{\vec{\mu}^T \vec{\mu}}. \quad (\text{Eq. 2})$$

185 $\Delta \mathbf{XCH}_4$ is then scaled by this pixel-specific scalar (f) and thus normalized by the albedo term, similar to the per-pixel
186 normalization in previous hyperspectral analysis (Kraut et al., 2005). The premise to launch the matched-filter algorithm is the
187 accurate knowledge of the response of the instrument spectra to the methane absorption nature. To this end, the objective is to
188 gain the best fit between the simulated and reference spectra. An initial step is thus conducted to update the spectral calibration
189 for the channels within the 2100 - 2400 nm window, in which the channel wavelength centre and width are updated for each
190 across-track position in each scene. Other details are illustrated in previous attempts (Foote et al., 2020; Guanter et al., 2021;
191 Irakulis-Loitxate et al., 2022).

192 2.3 Two-tiered attribution of methane hotspots and plumes

193 In the first tier of our framework, we apply visual inspection to identify methane hotspots using the TROPOMI-based methane
194 retrievals. The transformation from visual inspection to automatic recognition would significantly advance long-term, global
195 methane monitoring. However, no satisfactory set of criteria was found that could be suitable for this study. This was mainly
196 because, in localized regions, methane budgets respond to the changes in not only super-emitters but also complex external
197 factors (e.g., meteorology, topography, and background concentrations). Similar compromises are also adopted in previous
198 studies. Therefore, automatic recognition enabled by artificial intelligence would play an essential role in a versatile spaceborne
199 architecture for long-term, global methane monitoring (Ouerghi et al., 2021; Paoletti et al., 2018; Yang et al., 2018; Yu et al.,
200 2017; Zhang et al., 2018).

201 Regarding the identified methane hotspots, we utilize a Boolean mask to select plume-influenced pixels downwind of the
202 source. The background distribution (mean \pm standard deviation) is defined by an upwind sample of the measured columns, in
203 which the hourly wind field data come from the ERA5 reanalysis dataset produced by the European Centre for Medium-Range
204 Weather Forecasts (ECMWF) (Hoffmann et al., 2019). We then sample the surrounding (5 \times 5) pixels centred on each pixel
205 and compare the corresponding distributions to the background distribution based on a Student's t-test. Pixels with a
206 distribution substantially higher than the background at a confidence level of 95% are assigned to the plume. More details in
207 the Boolean plume mask can be found in previous studies (Pandey et al., 2019; Varon et al., 2018).

208 Regarding the identified regional hotspots, we also apply visual inspection to search for plumes within their surrounding 30
209 km scales (i.e., corresponding to the swath width of PRISMA) in the second tier of our framework (Irakulis-Loitxate et al.,
210 2021; Lauvaux et al., 2022; Martin et al., 2018; Varon et al., 2020). To date, it is still challenging to distinguish methane
211 plumes in hyperspectral images using full physically-based algorithms. The main cause is potential methane retrieval artifacts
212 from hyperspectral satellites that are spatially correlated to surface features. Specifically, we manually search for methane
213 enhancement pixels with gas-plume-like shapes, i.e., high methane enhancements progressively decreasing downwind. The
214 resulting pixels are subsequently compared to the spectral radiance data at the 2300 nm absorption feature sensitive to low
215 surface albedos. In this way, the fake positives due to specific surface features are prevented. On this basis, the candidate pixels
216 are overlaid over simultaneous (i.e., hourly) wind fields and high-resolution imageries in individual scenes. They would be
217 considered to be true plumes if they roughly align with simultaneous wind direction and originate from explicit infrastructures.
218 Here the high-resolution satellite imageries are taken from the Google Map. The hourly wind field data also come from the
219 ERA5 reanalysis dataset. Finally, we manually draw polygons to mask such resulting plumes. As preparation for plume
220 emission quantification, we remove the background using the threshold of the median values of the scenes.

221 These satellite imageries allow us to categorize methane plumes within narrow spatial scales between 50 to 500 m², such as
222 O&G extraction platforms, storage tanks, and compressor stations. They even enable the attribution of plumes to specific
223 emission ports in individual sources due to their very high resolution. Furthermore, we could name them based on points of
224 interest in the Google Map. On this basis, such sources could be visually retrospected via long-term, high-resolution (i.e., 10
225 m) satellite images from the Sentinel-2 mission (Ehret et al., 2021; Varon et al., 2021). Their key details, like ages and statuses
226 (e.g., active or inactive), are thus collected reliably. Note that, regarding such information, national reports are typically
227 credible but inaccessible, particularly in global missions. In addition, it should be highlighted that, in high source regions, such
228 as megacities, there are likely super-emitters that are undetectable following our method. Other causes are discussed in
229 uncertainty analysis in Supplement Information.

230 **2.4 Two-tiered quantification of methane emissions**

231 In our framework, we calculate the total excess mass of methane in kilograms in the detected hotspots (in the first tier) and
232 plumes (in the second tier) using the so-called integrated mass enhancement (IME) model (Frankenberg et al., 2016; Varon et
233 al., 2018). To make conservative estimates, we define the background levels as the 10% of the average methane concentrations

234 in the TROPOMI-based and PRISMA-based scenes (Figs. 1b ~ 1g) (Frankenberg et al., 2016; Varon et al., 2018). On this
235 basis, we eliminate the interferences from the background concentrations and calculate IMEs as the methane masses of the
236 masked hotspots and plumes.

237 Overall, this method links the emission rate (\mathbf{Q}) with the measured IME via the residence time of methane (\mathbf{IME}/\mathbf{Q}). This
238 residence time relies on an effective wind speed (\mathbf{U}_{eff}) and a characteristic plume size (\mathbf{L}) as follows:

239
$$\mathbf{Q} = \frac{\mathbf{U}_{\text{eff}} \cdot \mathbf{IME}}{\mathbf{L}}. \text{ (Eq. 3)}$$

240 Specifically, the **IME** and **L** can be inferred from the observations of the hotspots or plumes. During this process, we carefully
241 apply a Boolean plume mask that separates the pixels (\mathbf{i}) with notable signals ($\Delta\Omega_i$) from background pixels and thus defines
242 the total areas ($\sum_{i=1}^N A_i$) of the hotspots or plumes. The **L** is defined as the square root of the total plume areas. Hence, the **IME**
243 is calculated as follows:

244
$$\mathbf{IME} = \sum_{i=1}^N \Delta\Omega_i A_i. \text{ (Eq. 4)}$$

245 In the first tier of our framework, the effective wind speed (\mathbf{U}_{eff}) is defined as the 10-m wind speed \mathbf{U}_{10} obtained from the
246 ERA5 reanalysis dataset. According to the detected hotspot, the value at the nearest hour and location are used.

247 In the second tier of our framework, we apply an ensemble of large eddy simulations (LES) to establish an empirical, linear
248 relationship between \mathbf{U}_{eff} and the measured 10-m wind speed \mathbf{U}_{10} as follows (Fig. S8)

249
$$\mathbf{U}_{\text{eff}} = 0.8602 \mathbf{In}(\mathbf{U}_{10}) + 1.1513. \text{ (Eq. 5)}$$

250 The configurations of these simulations, such as spatial resolution and precision, are comparable to our PRISMA data. Other
251 details in this methodology were described in Varon et al. (2018) (Varon et al., 2018).

252 We estimate the uncertainties of \mathbf{Q} by propagating the random errors in \mathbf{U}_{10} and **IME**. This processes have been described in
253 previous studies (Cusworth et al., 2019, 2021b; Irakulis-Loitxate et al., 2021). As shown in previous findings, the major error
254 source come from the \mathbf{U}_{10} term, which typically has a random error of 50%. On this basis, this error is integrated quadratically
255 with the standard error of the **IME**, the result of which can be treated as the final random error of \mathbf{Q} . The intrinsic errors of the
256 **IME** model are quantified in the following uncertain analysis. As demonstrated in the Supplementary Information, our
257 comprehensive uncertainty analysis establishes the robustness of our estimates, with uncertainties being entirely controllable
258 within a range of -70% (Table S1). Such uncertainties are also used and shown in Figs. 1 ~ 4.

259 **2.5 Uncertainty Analysis**

260 The objective of this work is to promote a two-tiered satellite constellation that can monitor global methane pledges. To better
261 understand the performance of our framework, we conduct comprehensive uncertain analysis. Note that the protocol of the
262 uncertain analysis on our framework we need to account for originates from previous studies (Irakulis-Loitxate et al., 2021;
263 Varon et al., 2020). Specifically, we require to account for the uncertainties in the TROPOMI-based and PRISMA-based
264 methane retrievals and subsequent emission estimates. Therein the operational TROPOMI-based methane retrieval products
265 have been evaluated strictly and proved to be reliable globally (except in low- and high-albedo and snow-covered areas)

266 (Lorente et al., 2021; Sha et al., 2021). In this work, we thus focus on three main sources of uncertainties, specifically including
267 (1) uncertainties in the PRISMA-based methane retrievals; (2) uncertainties in the TROPOMI-based methane emission
268 estimates; and (3) uncertainties in PRISMA-based methane emission estimates. During the analysis for the latter two uncertain
269 sources, we would further investigate the potential wind impacts on the methane emission estimates. Note that it remains
270 challenging to directly quantify the uncertainties in the wind fields across our cases due to the lack of measurements. We would
271 thus assess the variations in the methane emission estimates driven by distinct wind data. From such analysis, we could confirm
272 the reliable performance of our framework. Details can be found in Supplementary Information.

273 The detection limit of this framework depends mainly on the TROPOMI-based and PRISMA-based methane retrievals, which
274 have been well discussed in previous studies (Guanter et al., 2021; Hu et al., 2018). As the robust relationship between the
275 “minimum source” and the related methane enhancement developed by Jacob et al. (2016) and Guanter et al. (2021) shows,
276 the detection threshold for the TROPOMI instrument is 4000 kg/h with a wind speed of 5 km/h. Following the same
277 relationship for the PRISMA instrument, we estimate that a retrieval precision of 114 ppb (6.1% with the assumed background
278 concentration of 1850 ppb), such as in the case of the Hassi Messaoud site (Fig. S10e1), would lead to a detection limit of 800
279 kg/h for the same wind speed (analogous to the reported range of 500 ~ 900 kg/h) (Guanter et al., 2021; Irakulis-Loitxate et
280 al., 2022). Similar instruments and detection limits are generally comparable to emissions from anthropogenic sectors, like
281 O&G and coal mines in this study or landfills, agriculture, and waste management in previous studies (Lauvaux et al., 2022;
282 Maasakkers et al., 2023; Sadavarte et al., 2021). However, no conclusive evidence shows by far that short-term (e.g., daily)
283 satellite-based measurements with such detection limits can capture methane hotspots driven by natural sources (e.g., wetlands).
284 In contrast, long-term (e.g., year-round) satellite-based measurements with much higher detection limits have shown potential
285 for monitoring natural methane hotspots (Pandey et al., 2021).

286 **3 Results and discussions**

287 **3.1 Two-tiered imaging of global methane hotspots and super-emitters**

288 Figure 1 presents representative sets of methane hotspots and associated super-emitters across the United States, China, the
289 Middle East (Iraq and Kuwait), and North Africa (Algeria) via our two-tiered satellite constellation. Each group first clarifies
290 a methane-abundant region and further focuses on explicit super-emitters. Among them, five methane-abundant regions are
291 captured in Wattenberg (the United States), Yangquan (China), Rumaila (Iraq), Burgan (Kuwait), and Hassi Messaoud (Algeria)
292 (Fig. 1a and Table S1). These account for 4805 ~ 46138 kg/h methane emissions based on our daily first-tiered (i.e.,
293 TROPOMI-based) monitoring. From the perspective of a state-of-the-art global methane emission inventory (i.e.,
294 EDGARv6.0), such high values rank among the top 1% regarding emission intensities per unit area (km^2) (Fig. S1) (Crippa et
295 al., 2020). The Rumaila field, for example, is known as the largest oil field in Iraq (in terms of both reserves and yields). In
296 this work, it is found with a significant methane emission intensity exceeding 45000 kg/h (Fig. 1b). Besides the well-known

297 oil fields (Figs. 1c ~ 1f), methane hotspots have also emerged in developing coal mine fields such as the Yangquan field, which
298 exhibit comparable emission levels ($> 30000 \text{ kg/h}$) (Fig. 1g).

299 We attribute these methane enhancements to specific methane plumes via the second-tiered (i.e., PRISMA-based) monitoring
300 (Figs. 1b1 ~ 1g2). There are substantial variations in the methane plumes' amounts, types, and magnitude, even in a single
301 methane-abundant region. For instance, in the Burgan field, the second-tiered monitoring detects up to eight methane plumes
302 in a handful of grids in the first-tiered monitoring (Figs. 1c1 ~ 1c4 and 1d1 ~ 1d4). Such intensive distributions are also found
303 in previous region-oriented surveys in the Permian basin and California (Duren et al., 2019; Irakulis-Loitxate et al., 2021).
304 Together with high-definition images (Fig. S2), we find that such plumes originate from various sources, such as flares,
305 factories, and wells. A breakthrough is the capture of two distinctive plumes in an individual methane source with extremely
306 high emissions ($> 10000 \text{ kg/h}$), unprecedented in previous satellite-based exploration and only observable in aircraft surveys
307 (Fig. 1b1). Such precise distinctions benefit from the high resolution of the second-tiered monitoring, despite being limited by
308 the relatively higher detection threshold ($\sim 800 \text{ kg/h}$). Besides, factories and wells can also emit such evident plumes (Fig. 1c1
309 and Figs. 1e1 and 1e2). By comparison, other plumes are typically more diffuse but with comparable emission magnitude (\sim
310 $1000 \sim 7000 \text{ kg/h}$).

311 Note that the above results represent only snapshots at the overpass moments of the satellites (i.e., TROPOMI and PRISMA)
312 (Figure 1). Specifically, for a given set (including both a methane-abundant region and associated super-emitters), the overpass
313 timing of TROPOMI can be nearly concordant with that of PRISMA in some cases. For instance, within only two days (August
314 18th and 19th, 2021, November 15th and 17th, 2021), our two-tiered satellite constellation goes through the Hassi Messaoud
315 field and the Yangquan coal mine and provides in-depth views of methane budgets, including methane-abundant regions and
316 their drivers (Figs. 1e and 1g). Even, in just one day (July 7th, 2021), our two-tiered satellite constellation not only uncover
317 methane enhancements in the Wattenberg field (Fig. 1f) but also track them back to explicit methane super-emitters (Figs. 1f1
318 and 1f2). As expected, if we extend the monitoring window of our framework to years, more methane super-emitters are
319 subsequently captured (Fig. S3). Moreover, our framework via two-tiered satellite constellation paves an in-time way for
320 routine monitoring of global methane hotspots and associated super-emitters.

321 **3.2 Two-tiered verification of global methane super-emitters**

322 Four unexpected cases occur in Burgan (Iraq), Hassi Messaoud (Algeria), and Yangquan (China), potentially explainable if
323 we take mutual verification of the first- and second-tiered monitoring into consideration. First, an anomalous methane plume
324 is detected in the Burgan field (Fig. 1c4) of high emission magnitude ($> 1500 \text{ kg/h}$), notably exceeding typical O&G facilities,
325 from an elusive source (i.e., no clear source could be attributed) (Fig. S2). The long-term measurements of our two-tiered
326 satellite constellation intermittently, rather than accidentally, observe this abnormal plume (Figs. S4). Furthermore, uncertain
327 analysis (see Materials and Methods) helps to confirm this real plume. In particular, the methane plumes are clearly

328 uncorrelated with the surface brightness from space (Fig. S4). Consequently, the most likely hypothesis for this super-emitter
329 is methane leakage from gigantic O&G pipelines as shown in the Google Map (Fig. S2).
330 Second, we observe suspect trails of methane plumes above the storage tanks in the Burgan field (Fig. 1d4). Conceivably, the
331 technical noise driven by albedo effects bore the brunt, although it is believed to be corrected reliably (See Materials and
332 Methods). To this end, we apply a multi-spectral retrieval algorithm to eliminate this effect to a large extent. We utilize two
333 spectral bands to launch the matched-filtered algorithm separately: one that is highly sensitive to methane absorption (i.e.,
334 2300 nm) and another that is much less sensitive (i.e., 1700 nm) but exhibit similar surface and aerosol reflectance properties.
335 Figure S5 shows that the 2300 nm -driven matched-filtered algorithm result in noticeable methane vestiges above the storage
336 tanks, while the 1700 nm-driven algorithm does not. Consequently, we provide evidence that un-negligible methane emissions
337 ($> 3500 \text{ kg/h}$) may very well be the only explanation, likely related to fugitive methane leaks from the storage tanks. This has
338 previously only seen in aircraft-based surveys (Frankenberg et al., 2016). Therefore, our two-tiered outcomes indicate there
339 are more widespread methane leaks than have been previously detected. Note that the multi-spectral retrieval algorithm cannot
340 completely remove the albedo effects on our results. However, our methods could lead to targeted on-site re-inspection on
341 O&G fields worldwide.
342 Third, our framework detects a new methane super-emitter in the Hassi Messaoud field on December 7, 2021 (Fig. 1e4). By
343 revisiting historical satellite images in the second-tiered monitoring (Fig. S6), we could confirm that this super-emitter arose
344 between October 18th and November 12, 2021. These results indicate that monitoring of global methane super-emitters can
345 attain monthly resolution via current satellite constellations alone. More satellites could capture changes during even shorter
346 time windows. Fourth, a distinct methane plume appears in a coal mine in a mountainous area (in the Yangquan field, China),
347 exceeding all of the detected O&G super-emitters regarding the emission rate ($> 7000 \text{ kg/h}$) (Fig. 1g1).
348 Figure 2 illustrates the extent to which the second-tier of our two-tiered satellite constellation explains the regional budget
349 detected by the first tier. Overall, the share of the regional budget due to the plumes ranges from 8.2% (Hassi Messaud) to 53.8
350 $\sim 65.9\%$ (Rumaila, Burgan, and Wattenberg). Note that such contribution estimates might occasionally exceed 100% mainly
351 owing to the different overpass time between the first- and second-tier monitoring. By comparison, the relatively low but still
352 significant contributions in the Hassi Messaoud field (8.2%) and Yangquan coal mine (35.7%) are partly due to the technical
353 limitation of our framework in detecting methane plumes on top of high background levels. Collectively, the heavy-tail law of
354 methane plume distributions, early reported for regional O&G fields (like the Permian basin and California) (Duren et al.,
355 2019; Irakulis-Loitxate et al., 2021), is possibly applicable worldwide. To further explore such a hypothesis, we extend the
356 temporal sample window of our two-tiered framework. Using year-round snapshots in the second tier of our framework, we
357 inspect the identified super-emitters (Figs. 1b ~ 1g) repeatedly and find more methane plumes as expected (Fig. S3). This
358 reinforces our hypothesis of the widespread occurrence of methane super-emitters.
359 Note that there are differences in the order of magnitude between the TROPOMI-based and PRISMA-based results. The main
360 cause is that the TROPOMI-based and PRIMSA-based results represent the methane emissions from different spatial scales.
361 The former results represent region-scale methane budgets, while the latter ones resolve the emission magnitude from the

362 individual methane super-emitter therein (Fig. 1). Although the latter results can explain a large fraction of the former ones
363 (Fig. 2), the gaps remain mainly due to different overpass time between the two-tiered results or sources still missed by the
364 PRIMSA-based results. In other words, closing the temporal gaps between the two tiers or improving the detection ability of
365 the second tier would help to reconcile the first- and second-tiered results.

366 A regional survey in a California field provides some useful data for evaluating our results, owing to its utilization of systematic
367 airborne measurements to detect and quantify methane super-emitters (Duren et al., 2019). The California survey aims to
368 provide the first view of methane super-emitters across the state. This survey was conducted with the Next Generation Airborne
369 Visible/Infrared Imaging Spectrometer (AVIRIS-NG), with 5 nm SWIR spectral sampling, 1.8 km view field, 3 m horizontal
370 resolution, and 3 km cruise altitude, and included five campaigns over several months from 2016 to 2018. Moreover, this
371 instrument is unique due to its high signal-to-noise ratio and is capable of characterizing methane super-emitters with emissions
372 as small as $2 \sim 10$ kg/h for typical surface winds of 5 m/s. The survey reports 1181 methane plumes, more than 500 times the
373 number of plumes reported by previous aerial studies (Englander et al., 2018), with a median emission intensity of 170 kg/h.
374 These results are thus used to directly evaluate the outcomes in the second tier (Fig. 3). Even though some regions of interest
375 in our study are far less well known than the California fields, their emission intensities are much higher. Specifically, the
376 plumes detected by the second-tiered monitoring have emission intensities (1142 \sim 11698 kg/h) that exceed the median value
377 in the California field.

378 Satellite observations taken over the Permian basin (one of the top O&G bases worldwide) from 2019 to 2020 (Irakulis-
379 Loitxate et al., 2021) provide additional comparison data (Fig. 3). The Permian survey took advantage of imaging spectroscopy
380 technologies to provide the first spaceborne region-scale and high-resolution survey of methane super-emitters in the Permian
381 basin. This survey acquired 30 hyperspectral images from three satellite missions, including Gaofen-5, ZY1, and PRISMA,
382 and focuses on an area of roughly 200×150 km² in the Delaware sub-basin of the Permian basin within several days (mostly
383 on four different dates: 15 May 2019, 1 November 2019, 29 December 2019, and 8 February 2020). More technical details on
384 these two surveys can be found in previous studies (Duren et al., 2019; Irakulis-Loitxate et al., 2021). Compared to the surveys
385 in the California field, those in the Permian basin reported a much higher number of strong methane super-emitters, the median
386 emission rates (1850 kg/h) much closer to ours (2888 kg/h). Collectively, although such comparisons are not quantitative due
387 to many differences in measurement characteristics (e.g., spatial resolution and detection limit), they provide context for the
388 emission magnitudes of the methane super-emitters we have identified and indicate that our results are within the range of
389 values obtained from field campaigns. More importantly, these results highlight the urgent need for global monitoring of
390 ‘nameless’ O&G facilities that possibly emit as much methane as the California field and Permian basin.

391 **3.3 Two-tiered challenges of national emission inventories**

392 Comparing emissions from our two-tiered approach with a state-of-the-art methane emission inventory (EDGARv6.0) for
393 2018, (Fig. 4), we find that our emission estimates using TROPOMI data over methane hotspots are roughly consistent with

394 the inventory, with biases ranging from -49.9% to 91.8% with an average bias of 63.2%. The exception is the Hassi Messaoud
395 field in Algeria where the O&G sector is in rapid development: here our estimate is 498.2% of the EDGARv6.0 inventory. On
396 the other hand, our estimates using PRISMA data over plumes are orders of magnitude greater than the EDGARv6.0 emissions.
397 This suggests that traditional emission inventories may have acceptable performance for methane abundant regions but may
398 grossly underestimate emission from methane super-emitters.

399 There are a number of possible explanations for the low estimates from EDGARv6.0. First, to establish bottom-up methane
400 emission inventories, we need to allocate area sources to regular grids based on spatial information, like nighttime lights (so-
401 called spatial proxies) (Geng et al., 2017). Outdated spatial proxies might explain the large divergence between our plant-based
402 estimates and the EDGARv6.0 (Fig. 1b1 and Fig. S7). Moreover, the EDGARv6.0 is designed for the year 2018, missing the
403 newly established O&G plants with high methane emissions. Second, in principle, conventional inventories directly miss high
404 emissions caused by abnormal operations (e.g., equipment failures) (Fig. 1c4 and Fig. S8) such as the O&G blowout (Pandey
405 et al., 2019). Generally, because of technical difficulties or safety risks, we have to compromise to measure such abnormal
406 emissions downwind rather than on sites. (Alvarez, 2018).

407 Third, the above divergence between our plant-based estimates and the EDGARv6.0 might also be explained by other causes
408 such as outdated emission factors. Empirically, a bottom-up inventory, once optimized by direct measurements, can raise total
409 methane emissions by ~ 60%, although source categories vary substantially (Alvarez, 2018). Besides, temporal variability
410 might also explain top-down and bottom-up differences in methane emission estimates. For instance, the peak emission rate
411 could exceed 40% higher than the average, which might occur in the middle afternoon due to specific processes, like episodic
412 venting from manual liquid unloading (Vaughn et al., 2018). This aligns with the sampling time of the satellites, thus biasing
413 bottom-up inventories. Collectively, it is necessary to carefully consider all factors affecting methane emissions, including
414 emission factor updating and spatiotemporal variations, in order to develop effective strategies for mitigating methane
415 emissions.

416 3.4 Implications for global methane monitoring

417 We have presented a two-tiered, space-based framework that can harmonize planet-scale and plant-level methane retrievals
418 (Fig. 5). We have demonstrated this framework with examples from around the world, with synergistic, proactive detections
419 on the methane-abundant regions and methane super-emitters across the United States, China, the Middle East (Iraq and
420 Kuwait), and North Africa (Algeria). We have located new methane super-emitters, tracked potential methane leakages from
421 storage tanks, and resolved multiple methane plumes from a single source. Such achievements are mostly unprecedented in
422 satellite surveys and only observed in aircraft campaigns. On this basis, our results suggest inventories miss unknown super-
423 emitters and underestimate emission magnitudes, partly due to a surge in the number of oil and gas (O&G) facilities and
424 widespread abnormalities in O&G operations. Our data prove that existing satellite missions can already lead to immediate,
425 proactive monitoring of global methane pledges, in contrast to existing surveys that have to focus on a priori methane-abundant

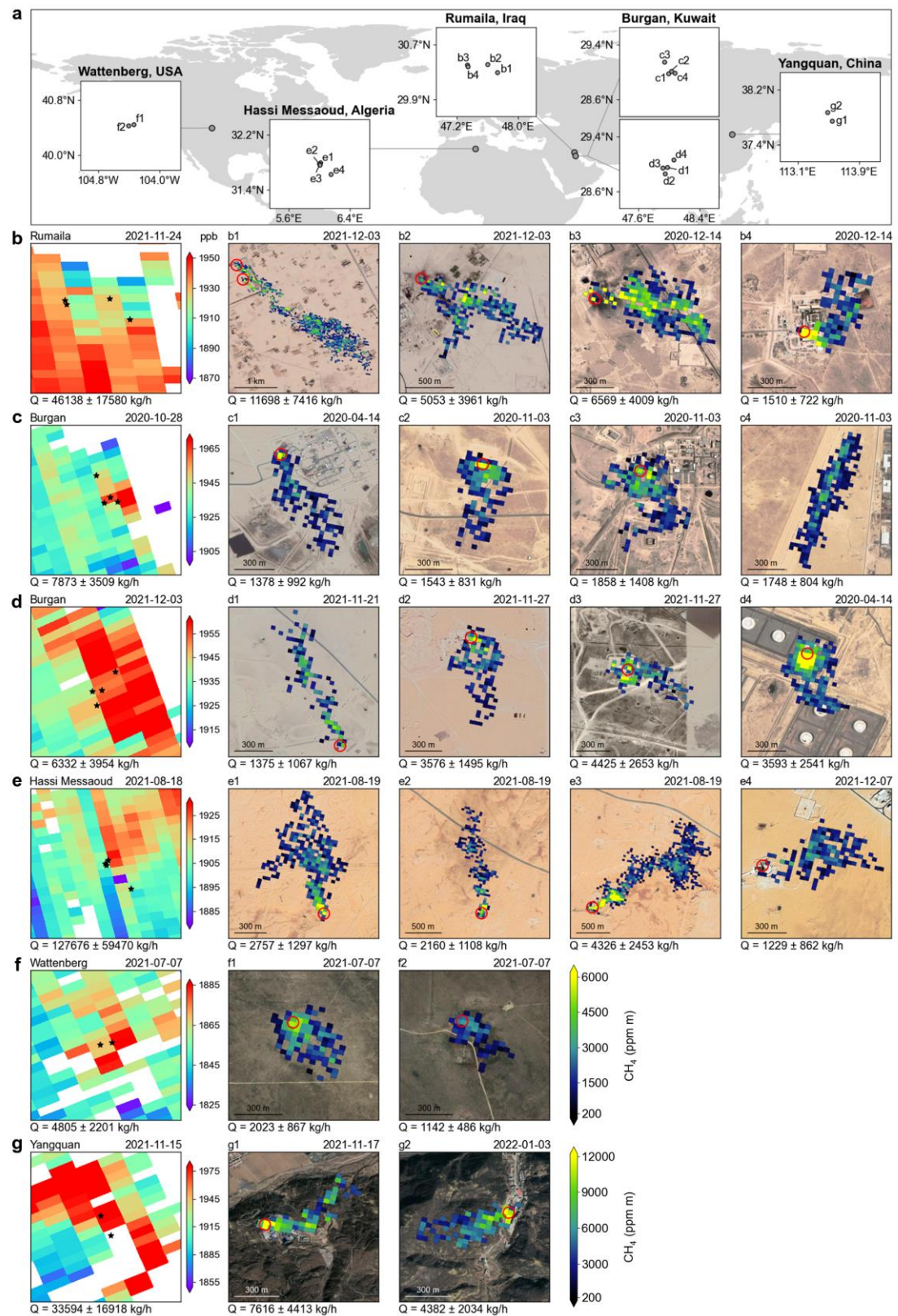
426 regions. While window for achieving the Paris target is rapidly closing, our approach can provide improved methane emission
427 estimates before the deployment of more advanced instruments, which can also be integrated into our system, like MethaneSAT
428 and SBG in the United States, EnMAP in Germany, a new version of GF-5 in China, and, later, the European Space Agency's
429 CHIME from 2025 to 2030 (Cusworth et al., 2019).

430 It should be noted that the multi-tiered framework is extremely flexible. (Fig. 5). First, it can harmonize multiple satellites.
431 The potential representatives include upcoming official missions (e.g., the GF-5) (Irakulis-Loitxate et al., 2021), current private
432 constellations (e.g., the GHGSat series) (Jervis et al., 2021; Varon et al., 2020), and explorable multispectral products (e.g.,
433 the Worldview-3 and Sentinel-2) (Sánchez-García et al., 2021). Second, the framework is not confined to satellites and can be
434 expanded by integrating in situ (e.g., Global Atmosphere Watch Programme) (World Meteorological Organization, 2022),
435 aircraft, and unmanned aerial vehicles (UAVs) (Cusworth et al., 2020; Gålfalk et al., 2021; Tuzson et al., 2020). Note that such
436 a multi-tiered framework based on multiple satellites, aircrafts, and UAVs will provide greater spatial coverages and more
437 frequent revisits. This flexibility will provide effective, efficient, and economic monitoring of global methane pledges, though
438 this will require careful balancing of coverage and resolution between instruments. This will be the topic of our next study.
439 Third, nighttime methane monitoring is important because abnormal leakages or pulses might also occur during nighttime
440 (Plant et al., 2022; Poindexter et al., 2016). In these events, LIDAR instruments (e.g., MERLIN) (Ehret et al., 2017) can retrieve
441 methane fluxes day and night at all latitudes, in all-seasons, and in all-weather. Fourth, better characterizing methane vertical
442 profiles would help to optimize our analysis, by minimizing the uncertainties in tropospheric air mass factors and subsequent
443 methane enhancements. Finally, rapid advances in artificial intelligence (AI) techniques can significantly speed up the
444 detection of faint signals from methane enhancements, and to significantly optimize data-driven algorithms of methane
445 emission estimates (Reichstein et al., 2019; Yuan et al., 2020). In principle, subsequent mitigation of such super-emitters via
446 routine maintenances, leak detections, or emergent repairs can provide effective, efficient, and economic solutions toward the
447 Paris target (Mayfield et al., 2017).

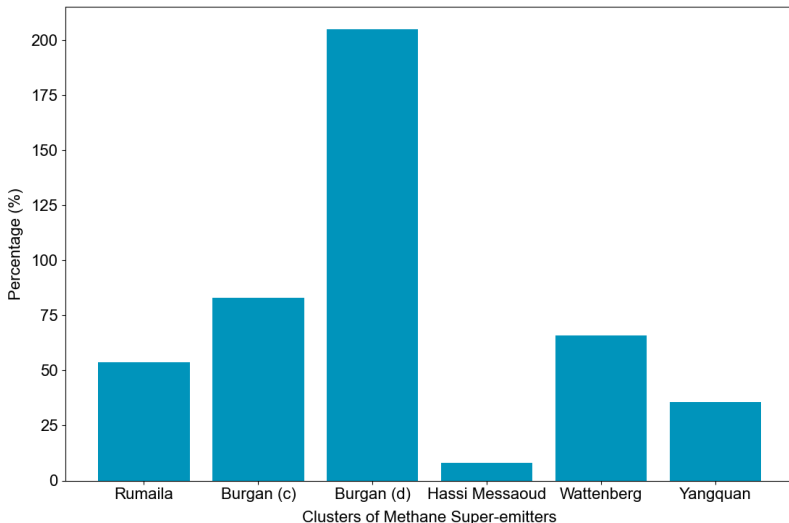
448 These outcomes have important ramifications for low- and middle-income countries. World powers, like the United States and
449 European Union, lead new national methane pledges. They are separately on the way to creating vast operational infrastructures
450 to monitor ambitious climate goals. Still, large gaps remain in coverage. This is especially true for low- and middle-income
451 countries, where tight budgets dim the hopes for filling these gaps by 2030, while methane emissions are likely to rise as
452 countries continue to develop. In this context, the present framework can serve as a cost-effective component of the global
453 methane monitoring network and thus support fair climate negotiations between countries.

454 This framework harmonizes global-scale and high-resolution methane retrievals, with a dual focus on mapping region-scale
455 and plant-level drivers. In this work, the framework reconciles the spacious swath of TROPOMI (i.e., ~ 2600 km) with the
456 high resolution of PRISMA (i.e., $30 \times 30 \text{ m}^2$), in contrast to conventional satellite-based surveys that were of either insufficient
457 samplings or narrow views. Looking forward, developments of Earth's monitoring platforms (e.g., satellites, aircrafts, and
458 UAVs) and AI will continue to strengthen the performance of methane plume retrievals and emission estimates. On eve of the

459 Paris target, at least while a super methane satellite with spacious swath, high resolution, and agile analysis is not in place, our
460 multi-tiered satellite constellation has important implications for measuring global methane pledges.

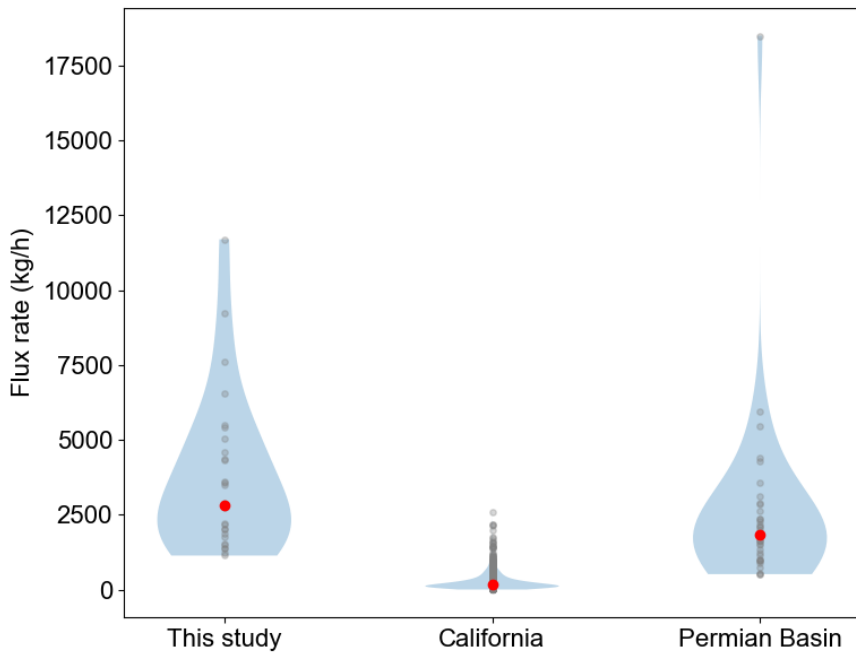


462 **Fig. 1. Methane hotspots and associated super-emitters across the United States, China, Iraq, Kuwait, and Algeria via**
463 **the two-tiered daily satellite constellation. (a)** Methane-abundant regions and associated super-emitters are captured by the
464 TROPOMI and PRISMA, respectively. Their locations are marked by black rectangles and dots. Their names are obtained
465 from the Google Map, and are usually the names of the nearest O&G fields and coal mines. **(b ~ g)** Each row presents a
466 methane-abundant region and the super-emitters detected within it (b1 ~ b4, c1 ~ c4, d1 ~ d4, e1 ~ e4, f1 ~ f2, and g1 ~ g2).
467 For each super-emitter (five-pointed stars), the overpass moments of the two-tiered satellite constellation and the consequent
468 emission estimate are presented. The base maps were obtained from © Google Map. The second color bar for the PRISMA is
469 suitable for the super-emitters in China, while the first applies for other countries. Plume sources in the PRISMA results are
470 marked by red circles.



471

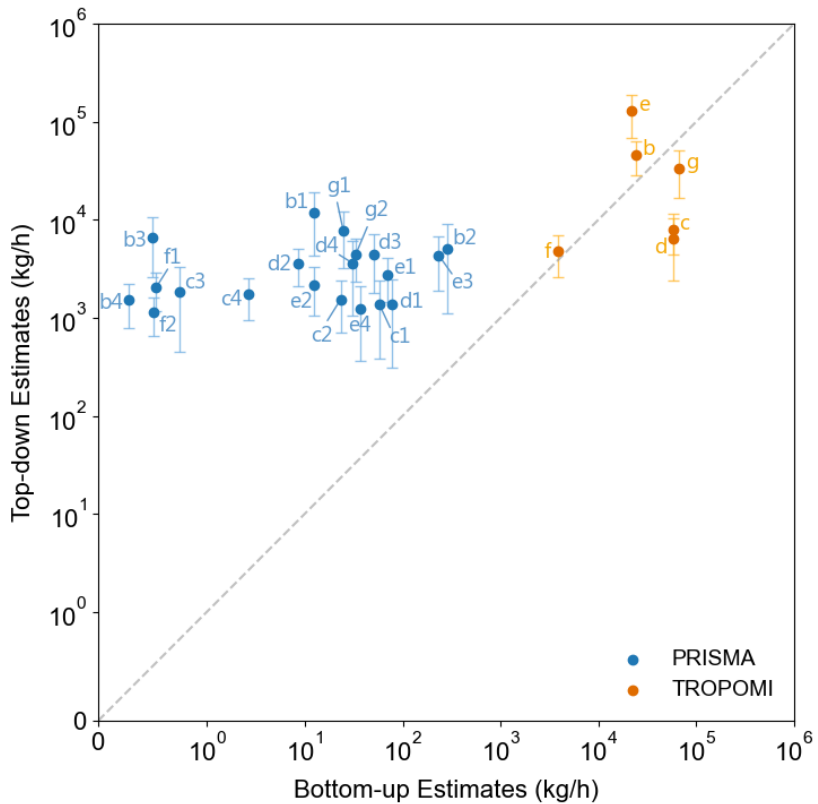
472 **Fig. 2. High contributions of methane super-emitters to corresponding regional methane budgets.**



473

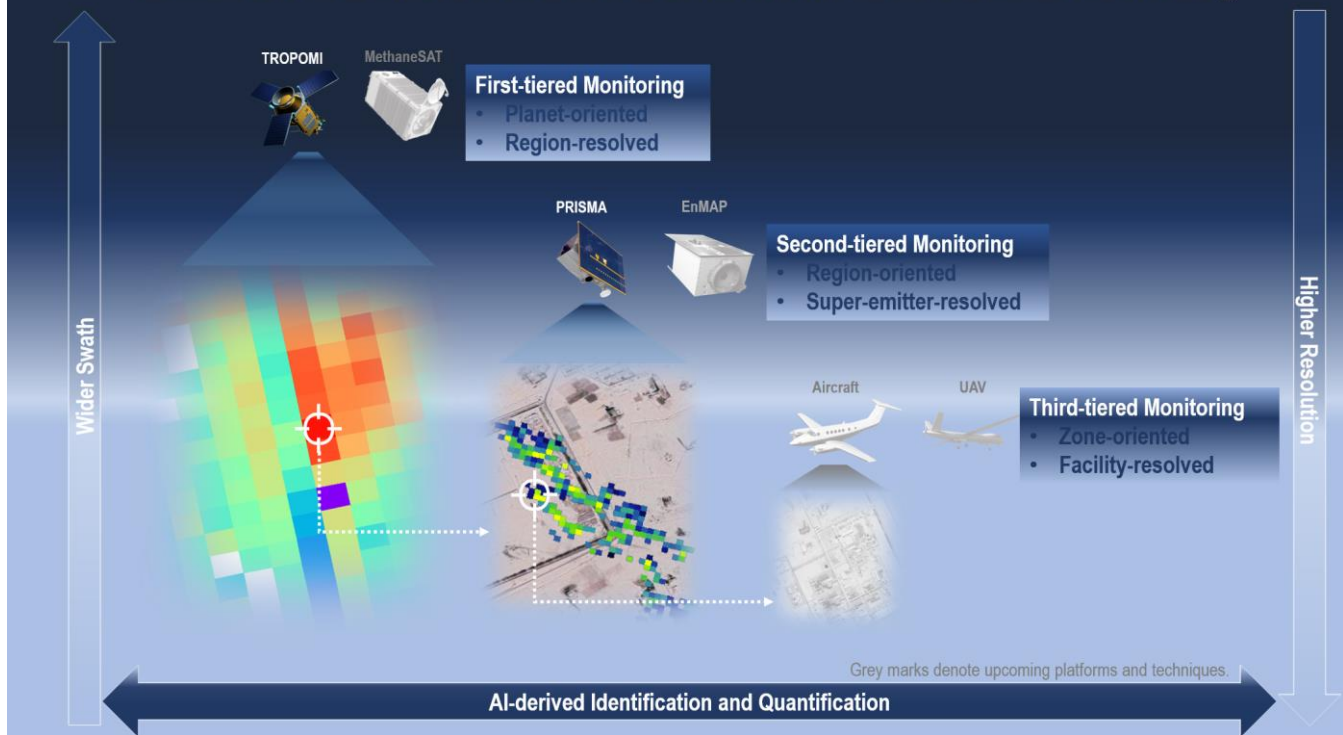
474 **Fig. 3. Comparison of emission estimates of methane plumes between surveys.** The surveys for the California field and
 475 Permian basin are selected as the references. They report 1181 and 39 methane plumes, while our second-tiered survey attempts
 476 29 plumes. Violin plots show statistical distributions of methane plume emission rates for these surveys. For each survey, the
 477 grey dots refer to the emission rates of the individual plumes and the red dot represents the median value. The shading
 478 represents the number distribution of the methane plumes with different emission rates.

479



480
481 **Fig. 4. Two-tiered emission estimates versus bottom-up emission inventories.** We first interpolate the bottom-up emission
482 inventories into the resolution consistent with our two-tiered results. On this basis, the bottom-up emission rates in the grids
483 that the detected hotspots and plumes cover are summed up to compare with the results. The detected hotspots (yellow dots)
484 and plumes (blue dots) correspond to those as shown in Fig. 1. The 1:1 line is shown by grey dashes.

Multi-tiered Satellite Constellation for Immediate Global Methane Monitoring



485

486 **Fig. 5. Multi-tiered satellite framework for immediate global methane monitoring.** The images of the TROPOMI,
487 MethaneSAT, PRISMA, and EnMAP are obtained from <http://www.tropomi.eu/>, <https://www.methanesat.org>,
488 <https://www.asi.it/en/earth-science/prisma/>, and <https://www.enmap.org/>, respectively. The methane maps from the
489 TROPOMI and PRISMA refer to the results in Figs. 1e and 1b1. The grey marks indicate upcoming platforms (i.e.,
490 MethaneSAT and EnMAP) and techniques (e.g., AI techniques that can optimize the identification and quantification of
491 methane super-emitters).

493 **Table 1. Spaceborne measurements for global methane monitoring.**

Satellite	Coverage/ Swath	Pixel Size (km ²)	SWIR (nm)	Spectral Resolution (nm)	Overpass (Local Time)	Period	Reference
SCIAMACHY	960 km	30 × 60	1630–1670	1.4	10:00	2002–2012	(Frankenberg et al., 2006)
GOSAT	790 km	10 × 10	1630–1700	0.06	13:00	2009–present	(Kuze et al., 2016)
GOSAT-2	1000 km	10 × 10	1630–1700, 2330–2380	0.06	13:00	2018–present	(Suto et al., 2021)
TROPOMI	2600 km	5.5 × 7, 7 × 7	2305–2385	0.25	13:30	2017–present	(Butz et al., 2012)
Sentinel-3	1420 km	0.5 × 0.5	1580–1640, 2230–2280	0.025	10:00	2016–present	(Pandey et al., 2022)
GHGSat	12 × 12 km ²	0.05 × 0.05	1600–1700	0.3–0.7	9:30	2016–present	(Varon et al., 2018)
PRISMA	30 × 30 km ²	0.03 × 0.03	1600–1700, 2200–2500	10	10:30	2019–present	(Guanter et al., 2021)
GF-5	60 × 60 km ²	0.03 × 0.03	2100–2400	10	13:30	2018–present	(Irakulnis-Loitxate et al., 2022)
ZY1	60 × 60 km ²	0.03 × 0.03	2100–2400	10	10:50		(Irakulnis-Loitxate et al., 2022)
Landsat-8	185 × 185 km ²	0.03 × 0.03	2300	200	10:50	2013–present	(Ehret et al., 2022)
Sentinel-2	290 km	0.02 × 0.02	1610, 2190	200	10:30	2015–present	(Varon et al., 2021)
Worldview-3	66.5 × 112 km ²	0.0037 × 0.0037	2295–2365	50	10:30	2014–present	(Sánchez-García et al., 2021)
EnMAP	30 × 30 km ²	0.03 × 0.03	1600–1700, 2200–2450	10	11:00	2020–present	(Cusworth et al., 2019)
EMIT	80 km	0.06 × 0.06	1600–1700, 2200–2510	7.4		2022–present	(EMIT, 2023)

495 **Data availability.**

496 The operational TROPOMI product is available at <https://scihub.copernicus.eu/>, <https://www.temis.nl/emissions/data.php>. The
497 PRISMA data are publicly available to registered users at <https://prisma.asi.it/>. The WRF-CHEM model code is available at
498 <https://ruc.noaa.gov/wrf/wrf-chem/>. All Sentinel-2 satellite data are publicly available through the Copernicus Open Access
499 Hub (<https://scihub.copernicus.eu/>). The HITRAN line spectra is publicly available through the HITRANonline database
500 (<https://hitran.org/>). The ERA5 data come from <https://www.ecmwf.int/en/forecasts/datasets/reanalysis-datasets/era5>. The
501 EDGARv6.0 dataset comes from <https://edgar.jrc.ec.europa.eu/gallery?release=v60ghg&substance=CH4§or=TOTALS>.

502 **Code availability.**

503 The codes are available upon request to corresponding author.

504 **Supplementary information.**

505 Supplementary information accompanies this paper.

506 **Author contributions.**

507 P. L. designed this study and wrote the manuscript. P. L. and Y. W. developed the retrieval algorithm. P. L., Y. W., X. G., Y.
508 H., and Y. P. performed the data analysis. S. Y., A.B., D. R., and J. H. S. contributed to the manuscript.

509 **Competing interests.**

510 The authors declare no competing interests.

511 **Acknowledgements.**

512 We thank ESA and the S-5P/TROPOMI team for the great work on initiating and realizing TROPOMI data. We also thank
513 the Italian Space Agency for the great work on the PRISMA data. This study is funded by National Natural Science Foundation
514 of China (No. 22006030, 72361137007, 22076172, 21577126 and 41561144004), Science and Technology Program of Hebei
515 Province (22343702D), Science and Technology Project of Hebei Education Department (BJ2020032 and QN2019184), Basic
516 Scientific Research Foundation of Hebei (KY2021024), Initiation Fund of Hebei Agricultural University (412201904 and
517 YJ201833), the Department of Science and Technology of China (No. 2016YFC0202702, 2018YFC0213506 and
518 2018YFC0213503), and National Research Program for Key Issues in Air Pollution Control in China (No. DQGG0107).

519 **References**

520 Allen, D. T., Torres, V. M., Thomas, J., Sullivan, D. W., Harrison, M., Hendler, A., Herndon, S. C., Kolb, C. E., Fraser, M.
521 P., Hill, A. D., Lamb, B. K., Miskimins, J., Sawyer, R. F. and Seinfeld, J. H.: Measurements of methane emissions at natural
522 gas production sites in the United States, *Proc. Natl. Acad. Sci.*, 110(44), 17768–17773, doi:10.1073/pnas.1304880110,
523 2013.

524 Allen, F., Gokul, I., Leon, C., James, E., Nathan, H., Haewon, M., Joeri, R., Reed, S., Jameel, A., R., A. G., Jared, C., Minji,
525 J., James, M., Anupriya, M. and Wenjing, S.: Can Paris pledges avert severe climate change?, *Science* (80-.), 350(6265),
526 1168–1169, doi:10.1126/science.aad5761, 2015.

527 Alvarez, R. A.: Assessment of methane emissions from the U.S. oil and gas supply chain, *Science* (80-.), 361(6398), 186–
528 188, doi:10.1126/science.aar7204, 2018.

529 Alvarez, R. A., Zavala-Araiza, D., Lyon, D. R., Allen, D. T., Barkley, Z. R., Brandt, A. R., Davis, K. J., Herndon, S. C.,
530 Jacob, D. J. and Karion, A.: Assessment of methane emissions from the US oil and gas supply chain, *Science* (80-.),
531 361(6398), 186–188, 2018.

532 Butz, A., Hasekamp, O. P., Frankenberg, C. and Aben, I.: Retrievals of atmospheric CO₂ from simulated space-borne
533 measurements of backscattered near-infrared sunlight: accounting for aerosol effects, *Appl. Opt.*, 48(18), 3322–3336,
534 doi:10.1364/AO.48.003322, 2009.

535 Butz, A., Guerlet, S., Hasekamp, O., Schepers, D., Galli, A., Aben, I., Frankenberg, C., Hartmann, J.-M., Tran, H., Kuze, A.,
536 Keppel-Aleks, G., Toon, G., Wunch, D., Wennberg, P., Deutscher, N., Griffith, D., Macatangay, R., Messerschmidt, J.,
537 Notholt, J. and Warneke, T.: Toward accurate CO₂ and CH₄ observations from GOSAT, *Geophys. Res. Lett.*, 38(14),
538 doi:<https://doi.org/10.1029/2011GL047888>, 2011.

539 Butz, A., Galli, A., Hasekamp, O., Landgraf, J., Tol, P. and Aben, I.: TROPOMI aboard Sentinel-5 Precursor: Prospective
540 performance of CH₄ retrievals for aerosol and cirrus loaded atmospheres, *Remote Sens. Environ.*, 120, 267–276,
541 doi:<https://doi.org/10.1016/j.rse.2011.05.030>, 2012.

542 Conley, S., Franco, G., Faloona, I., Blake, D. R., Peischl, J. and Ryerson, T. B.: Methane emissions from the 2015 Aliso
543 Canyon blowout in Los Angeles, CA, *Science* (80-.), 351(6279), 1317–1320, 2016.

544 Crippa, M., Solazzo, E., Huang, G., Guizzardi, D., Koffi, E., Muntean, M., Schieberle, C., Friedrich, R. and Janssens-
545 Maenhout, G.: High resolution temporal profiles in the Emissions Database for Global Atmospheric Research, *Sci. Data*,
546 7(1), 121, doi:10.1038/s41597-020-0462-2, 2020.

547 Cusworth, D. H., Jacob, D. J., Varon, D. J., Chan Miller, C., Liu, X., Chance, K., Thorpe, A. K., Duren, R. M., Miller, C. E.,
548 Thompson, D. R., Frankenberg, C., Guanter, L. and Randles, C. A.: Potential of next-generation imaging spectrometers to
549 detect and quantify methane point sources from space, *Atmos. Meas. Tech.*, 12(10), 5655–5668, doi:10.5194/amt-12-5655-
550 2019, 2019.

551 Cusworth, D. H., Duren, R. M., Yadav, V., Thorpe, A. K., Verhulst, K., Sander, S., Hopkins, F., Rafiq, T. and Miller, C. E.:
552 Synthesis of Methane Observations Across Scales: Strategies for Deploying a Multitiered Observing Network, *Geophys.*
553 *Res. Lett.*, 47(7), e2020GL087869, doi:<https://doi.org/10.1029/2020GL087869>, 2020.

554 Cusworth, D. H., Duren, R. M., Thorpe, A. K., Olson-Duvall, W., Heckler, J., Chapman, J. W., Eastwood, M. L.,
555 Helmlinger, M. C., Green, R. O., Asner, G. P., Dennison, P. E. and Miller, C. E.: Intermittency of Large Methane Emitters in
556 the Permian Basin, *Environ. Sci. Technol. Lett.*, 8(7), 567–573, doi:[10.1021/acs.estlett.1c00173](https://doi.org/10.1021/acs.estlett.1c00173), 2021a.

557 Cusworth, D. H., Duren, R. M., Thorpe, A. K., Pandey, S., Maasakkers, J. D., Aben, I., Jervis, D., Varon, D. J., Jacob, D. J.
558 and Randles, C. A.: Multisatellite Imaging of a Gas Well Blowout Enables Quantification of Total Methane Emissions,
559 *Geophys. Res. Lett.*, 48(2), e2020GL090864, 2021b.

560 Deng, Z., Ciais, P., Tzompa-Sosa, Z. A., Saunois, M., Qiu, C., Tan, C., Sun, T., Ke, P., Cui, Y., Tanaka, K., Lin, X.,
561 Thompson, R. L., Tian, H., Yao, Y., Huang, Y., Lauerwald, R., Jain, A. K., Xu, X., Bastos, A., Sitch, S., Palmer, P. I.,
562 Lauvaux, T., d'Aspremont, A., Giron, C., Benoit, A., Poulter, B., Chang, J., Petrescu, A. M. R., Davis, S. J., Liu, Z., Grassi,
563 G., Albergel, C., Tubiello, F. N., Perugini, L., Peters, W. and Chevallier, F.: Comparing national greenhouse gas budgets
564 reported in UNFCCC inventories against atmospheric inversions, *Earth Syst. Sci. Data*, 14(4), 1639–1675, doi:[10.5194/essd-14-1639-2022](https://doi.org/10.5194/essd-14-1639-2022), 2022.

565 Duren, R. M., Thorpe, A. K., Foster, K. T., Rafiq, T., Hopkins, F. M., Yadav, V., Bue, B. D., Thompson, D. R., Conley, S.
566 and Colombi, N. K.: California's methane super-emitters, *Nature*, 575(7781), 180–184, 2019.

567 Ehret, G., Bousquet, P., Pierangelo, C., Alpers, M., Millet, B., Abshire, J. B., Bovensmann, H., Burrows, J. P., Chevallier, F.,
568 Ciais, P., Crevoisier, C., Fix, A., Flamant, P., Frankenberg, C., Gibert, F., Heim, B., Heimann, M., Houweling, S.,
569 Hubberten, H. W., Jöckel, P., Law, K., Löw, A., Marshall, J., Agusti-Panareda, A., Payan, S., Prigent, C., Rairoux, P., Sachs,
570 T., Scholze, M. and Wirth, M.: MERLIN: A French-German Space Lidar Mission Dedicated to Atmospheric Methane,
571 *Remote Sens.*, 9(10), doi:[10.3390/rs9101052](https://doi.org/10.3390/rs9101052), 2017.

572 Ehret, T., Truchis, A. De, Mazzolini, M., Morel, J.-M., d'Aspremont, A., Lauvaux, T., Duren, R., Cusworth, D. and
573 Facciolo, G.: Global Tracking and Quantification of Oil and Gas Methane Emissions from Recurrent Sentinel-2 Imagery,
574 2021.

575 Ehret, T., De Truchis, A., Mazzolini, M., Morel, J.-M., d'Aspremont, A., Lauvaux, T., Duren, R., Cusworth, D. and
576 Facciolo, G.: Global Tracking and Quantification of Oil and Gas Methane Emissions from Recurrent Sentinel-2 Imagery,
577 *Environ. Sci. Technol.*, 56(14), 10517–10529, doi:[10.1021/acs.est.1c08575](https://doi.org/10.1021/acs.est.1c08575), 2022.

578 EMIT: Earth Surface Mineral Dust Source Investigation (EMIT), [online] Available from: <https://earth.jpl.nasa.gov/emit/>,
579 2023.

580 Englander, J. G., Brandt, A. R., Conley, S., Lyon, D. R. and Jackson, R. B.: Aerial Interyear Comparison and Quantification
581 of Methane Emissions Persistence in the Bakken Formation of North Dakota, USA, *Environ. Sci. Technol.*, 52(15), 8947–
582 8953, doi:[10.1021/acs.est.8b01665](https://doi.org/10.1021/acs.est.8b01665), 2018.

584 Etminan, M., Myhre, G., Highwood, E. J. and Shine, K. P.: Radiative forcing of carbon dioxide, methane, and nitrous oxide:
585 A significant revision of the methane radiative forcing, *Geophys. Res. Lett.*, 43(24), 12,612-614,623,
586 doi:<https://doi.org/10.1002/2016GL071930>, 2016.

587 Foote, M. D., Dennison, P. E., Thorpe, A. K., Thompson, D. R., Jongaramrungruang, S., Frankenberg, C. and Joshi, S. C.:
588 Fast and Accurate Retrieval of Methane Concentration From Imaging Spectrometer Data Using Sparsity Prior, *IEEE Trans.*
589 *Geosci. Remote Sens.*, 58(9), 6480–6492, doi:10.1109/TGRS.2020.2976888, 2020.

590 Frankenberg, C., Meirink, J. F., Bergamaschi, P., Goede, A. P. H., Heimann, M., Körner, S., Platt, U., van Weele, M. and
591 Wagner, T.: Satellite chartography of atmospheric methane from SCIAMACHY on board ENVISAT: Analysis of the years
592 2003 and 2004, *J. Geophys. Res. Atmos.*, 111(D7), doi:<https://doi.org/10.1029/2005JD006235>, 2006.

593 Frankenberg, C., Thorpe, A. K., Thompson, D. R., Hulley, G., Kort, E. A., Vance, N., Borchardt, J., Krings, T., Gerilowski,
594 K., Sweeney, C., Conley, S., Bue, B. D., Aubrey, A. D., Hook, S. and Green, R. O.: Airborne methane remote measurements
595 reveal heavy-tail flux distribution in Four Corners region, *Proc. Natl. Acad. Sci.*, 113(35), 9734 LP – 9739,
596 doi:10.1073/pnas.1605617113, 2016.

597 Gålfalk, M., Nilsson Påledal, S. and Bastviken, D.: Sensitive Drone Mapping of Methane Emissions without the Need for
598 Supplementary Ground-Based Measurements, *ACS Earth Sp. Chem.*, 5(10), 2668–2676,
599 doi:10.1021/acsearthspacechem.1c00106, 2021.

600 Ganesan, A. L., Schwietzke, S., Poulter, B., Arnold, T., Lan, X., Rigby, M., Vogel, F. R., van der Werf, G. R., Janssens-
601 Maenhout, G., Boesch, H., Pandey, S., Manning, A. J., Jackson, R. B., Nisbet, E. G. and Manning, M. R.: Advancing
602 Scientific Understanding of the Global Methane Budget in Support of the Paris Agreement, *Global Biogeochem. Cycles*,
603 33(12), 1475–1512, doi:<https://doi.org/10.1029/2018GB006065>, 2019.

604 Geng, G., Zhang, Q., Martin, R. V., Lin, J., Huo, H., Zheng, B., Wang, S. and He, K.: Impact of spatial proxies on the
605 representation of bottom-up emission inventories: A satellite-based analysis., *Atmos. Chem. Phys.*, 17(6), 2017.

606 Guanter, L., Irakulis-Loitxate, I., Gorroño, J., Sánchez-García, E., Cusworth, D. H., Varon, D. J., Cogliati, S. and Colombo,
607 R.: Mapping methane point emissions with the PRISMA spaceborne imaging spectrometer, *Remote Sens. Environ.*, 265,
608 112671, doi:<https://doi.org/10.1016/j.rse.2021.112671>, 2021.

609 Hasekamp, O. P. and Butz, A.: Efficient calculation of intensity and polarization spectra in vertically inhomogeneous
610 scattering and absorbing atmospheres, *J. Geophys. Res. Atmos.*, 113(D20), doi:<https://doi.org/10.1029/2008JD010379>, 2008.

611 Hoffmann, L., Günther, G., Li, D., Stein, O., Wu, X., Griessbach, S., Heng, Y., Konopka, P., Müller, R., Vogel, B. and
612 Wright, J. S.: From ERA-Interim to ERA5: the considerable impact of ECMWF's next-generation reanalysis on Lagrangian
613 transport simulations, *Atmos. Chem. Phys.*, 19(5), 3097–3124, doi:10.5194/acp-19-3097-2019, 2019.

614 Hu, H., Landgraf, J., Detmers, R., Borsdorff, T., Aan de Brugh, J., Aben, I., Butz, A. and Hasekamp, O.: Toward Global
615 Mapping of Methane With TROPOMI: First Results and Intersatellite Comparison to GOSAT, *Geophys. Res. Lett.*, 45(8),
616 3682–3689, doi:<https://doi.org/10.1002/2018GL077259>, 2018.

617 Irakulis-Loitxate, I., Guanter, L., Liu, Y.-N., Varon, D. J., Maasakkers, J. D., Zhang, Y., Chulakadabba, A., Wofsy, S. C.,
618 Thorpe, A. K., Duren, R. M. and Others: Satellite-based survey of extreme methane emissions in the Permian basin, *Sci.*
619 *Adv.*, 7(27), eabf4507, doi:10.1126/sciadv.abf4507, 2021.

620 Irakulis-Loitxate, I., Guanter, L., Liu, Y.-N., Varon, D. J., Maasakkers, J. D., Zhang, Y., Chulakadabba, A., Wofsy, S. C.,
621 Thorpe, A. K., Duren, R. M. and Others: Satellite-based survey of extreme methane emissions in the Permian basin, *Sci.*
622 *Adv.*, 7(27), eabf4507, doi:10.1126/sciadv.abf4507, 2022.

623 Jacob, D. J., Turner, A. J., Maasakkers, J. D., Sheng, J., Sun, K., Liu, X., Chance, K., Aben, I., McKeever, J. and
624 Frankenberg, C.: Satellite observations of atmospheric methane and their value for quantifying methane emissions, *Atmos.*
625 *Chem. Phys.*, 16(22), 14371–14396, doi:10.5194/acp-16-14371-2016, 2016.

626 Jervis, D., McKeever, J., Durak, B. O. A., Sloan, J. J., Gains, D., Varon, D. J., Ramier, A., Strupler, M. and Tarrant, E.: The
627 GHGSat-D imaging spectrometer, *Atmos. Meas. Tech.*, 14(3), 2127–2140, doi:10.5194/amt-14-2127-2021, 2021.

628 Kraut, S., Scharf, L. L. and Butler, R. W.: The adaptive coherence estimator: a uniformly most-powerful-invariant adaptive
629 detection statistic, *IEEE Trans. Signal Process.*, 53(2), 427–438, doi:10.1109/TSP.2004.840823, 2005.

630 Kuze, A., Suto, H., Shiomi, K., Kawakami, S., Tanaka, M., Ueda, Y., Deguchi, A., Yoshida, J., Yamamoto, Y., Kataoka, F.,
631 Taylor, T. E. and Buijs, H. L.: Update on GOSAT TANSO-FTS performance, operations, and data products after more than
632 6 years in space, *Atmos. Meas. Tech.*, 9(6), 2445–2461, doi:10.5194/amt-9-2445-2016, 2016.

633 Lauvaux, T., Giron, C., Mazzolini, M., d'Aspremont, A., Duren, R., Cusworth, D., Shindell, D. and Ciais, P.: Global
634 assessment of oil and gas methane ultra-emitters, *Science* (80-.), 375(6580), 557–561, 2022.

635 Lorente, A., Borsdorff, T., Butz, A., Hasekamp, O., aan de Brugh, J., Schneider, A., Wu, L., Hase, F., Kivi, R., Wunch, D.,
636 Pollard, D. F., Shiomi, K., Deutscher, N. M., Velazco, V. A., Roehl, C. M., Wennberg, P. O., Warneke, T. and Landgraf, J.:
637 Methane retrieved from TROPOMI: improvement of the data product and validation of the first 2 years of measurements,
638 *Atmos. Meas. Tech.*, 14(1), 665–684, doi:10.5194/amt-14-665-2021, 2021.

639 Maasakkers, J. D., Varon, D. J., Elfarsdóttir, A., McKeever, J., Jervis, D., Mahapatra, G., Pandey, S., Lorente, A., Borsdorff,
640 T., Foorthuis, L. R., Schuit, B. J., Tol, P., van Kempen, T. A., van Hees, R. and Aben, I.: Using satellites to uncover large
641 methane emissions from landfills, *Sci. Adv.*, 8(32), eabn9683, doi:10.1126/sciadv.abn9683, 2023.

642 Marchese, A. J., Vaughn, T. L., Zimmerle, D. J., Martinez, D. M., Williams, L. L., Robinson, A. L., Mitchell, A. L.,
643 Subramanian, R., Tkacik, D. S., Roscioli, J. R. and Herndon, S. C.: Methane Emissions from United States Natural Gas
644 Gathering and Processing, *Environ. Sci. Technol.*, 49(17), 10718–10727, doi:10.1021/acs.est.5b02275, 2015.

645 Martin, Van, Damme, Lieven, Clarisse, Simon, Whitburn, Juliette, Hadji-Lazaro and Daniel: Industrial and agricultural
646 ammonia point sources exposed, *Nature*, 2018.

647 Masood, E. and Tollefson, J.: COP26 climate pledges: What scientists think so far, *Nature*, d41586-021-03034-z,
648 doi:10.1038/d41586-021-03034-z, 2021.

649 Mayfield, E. N., Robinson, A. L. and Cohon, J. L.: System-wide and Superemitter Policy Options for the Abatement of
650 Methane Emissions from the U.S. Natural Gas System, *Environ. Sci. Technol.*, 51(9), 4772–4780,
651 doi:10.1021/acs.est.6b05052, 2017.

652 Mikaloff, F. S. E. and Hinrich, S.: Rising methane: A new climate challenge, *Science* (80- .), 364(6444), 932–933,
653 doi:10.1126/science.aax1828, 2019.

654 Miller, S. M., Michalak, A. M., Detmers, R. G., Hasekamp, O. P., Bruhwiler, L. M. P. and Schwietzke, S.: China's coal mine
655 methane regulations have not curbed growing emissions, *Nat. Commun.*, 10(1), 1–8, 2019.

656 National Oceanic and Atmospheric Administration: Increase in atmospheric methane set another record during 2021,
657 [online] Available from: <https://www.noaa.gov/news-release/increase-in-atmospheric-methane-set-another-record-during-2021>, 2022.

659 Nisbet, E. G., Manning, M. R., Dlugokencky, E. J., Fisher, R. E., Lowry, D., Michel, S. E., Myhre, C. L., Platt, S. M., Allen,
660 G. and Bousquet, P.: Very Strong Atmospheric Methane Growth in the 4 Years 2014–2017: Implications for the Paris
661 Agreement, *Global Biogeochem. Cycles*, 33, 2019.

662 Nisbet, E. G., Fisher, R. E., Lowry, D., France, J. L., Allen, G., Bakkaloglu, S., Broderick, T. J., Cain, M., Coleman, M.,
663 Fernandez, J., Forster, G., Griffiths, P. T., Iverach, C. P., Kelly, B. F. J., Manning, M. R., Nisbet-Jones, P. B. R., Pyle, J. A.,
664 Townsend-Small, A., al-Shalaan, A., Warwick, N. and Zazzeri, G.: Methane Mitigation: Methods to Reduce Emissions, on
665 the Path to the Paris Agreement, *Rev. Geophys.*, 58(1), e2019RG000675, doi:<https://doi.org/10.1029/2019RG000675>, 2020.

666 Ocko, I. B., Sun, T., Shindell, D., Oppenheimer, M., Hristov, A. N., Pacala, S. W., Mauzerall, D. L., Xu, Y. and Hamburg, S.
667 P.: Acting rapidly to deploy readily available methane mitigation measures by sector can immediately slow global warming,
668 *Environ. Res. Lett.*, 16(5), 54042, doi:10.1088/1748-9326/abf9c8, 2021.

669 Ouerghi, E., Ehret, T., de Franchis, C., Facciolo, G., Lauvaux, T., Meinhardt, E. and Morel, J.-M.: Detection of methane
670 plumes in hyperspectral images from SENTINEL-5P by coupling anomaly detection and pattern recognition, *ISPRS Ann.*
671 *Photogramm. Remote Sens. Spat. Inf. Sci.*, V-3–2021, 81–87, doi:10.5194/isprs-annals-V-3-2021-81-2021, 2021.

672 Pandey, S., Gautam, R., Houweling, S., Van Der Gon, H. D., Sadavarte, P., Borsdorff, T., Hasekamp, O., Landgraf, J., Tol,
673 P. and Van Kempen, T.: Satellite observations reveal extreme methane leakage from a natural gas well blowout, *Proc. Natl.*
674 *Acad. Sci.*, 116(52), 26376–26381, 2019.

675 Pandey, S., Houweling, S., Lorente, A., Borsdorff, T., Tsivlidou, M., Bloom, A. A., Poulter, B., Zhang, Z. and Aben, I.:
676 Using satellite data to identify the methane emission controls of South Sudan's wetlands, *Biogeosciences*, 18(2), 557–572,
677 doi:10.5194/bg-18-557-2021, 2021.

678 Pandey, S., van Nistelrooij, M., Maasakers, J. D., Sutar, P., Houweling, S., Varon, D. J., Tol, P., Gains, D., Worden, J. and
679 Aben, I.: Daily detection and quantification of methane leaks using Sentinel-3: a tiered satellite observation approach with
680 Sentinel-2 and Sentinel-5p, , doi:10.48550/ARXIV.2212.11318, 2022.

681 Paoletti, M. E., Haut, J. M., Plaza, J. and Plaza, A.: A new deep convolutional neural network for fast hyperspectral image
682 classification, *ISPRS J. Photogramm. Remote Sens.*, 145, 120–147, doi:<https://doi.org/10.1016/j.isprsjprs.2017.11.021>, 2018.

683 Phil DeCola and WMO Secretariat: An Integrated Global Greenhouse Gas Information System (IG3IS), [online] Available
684 from: <https://public.wmo.int/en/resources/bulletin/integrated-global-greenhouse-gas-information-system-ig3is>, 2017.

685 Plant, G., Kort, E. A., Brandt, A. R., Chen, Y., Fordice, G., Gorchov Negron, A. M., Schwietzke, S., Smith, M. and Zavala-
686 Araiza, D.: Inefficient and unlit natural gas flares both emit large quantities of methane, *Science* (80-..), 377(6614), 1566–
687 1571, doi:10.1126/science.abq0385, 2022.

688 Poindexter, C. M., Baldocchi, D. D., Matthes, J. H., Knox, S. H. and Variano, E. A.: The contribution of an overlooked
689 transport process to a wetland's methane emissions, *Geophys. Res. Lett.*, 43(12), 6276–6284,
690 doi:<https://doi.org/10.1002/2016GL068782>, 2016.

691 Reichstein, M., Camps-Valls, G., Stevens, B., Jung, M., Denzler, J., Carvalhais, N. and Prabhat: Deep learning and process
692 understanding for data-driven Earth system science, *Nature*, 566(7743), 195–204, doi:10.1038/s41586-019-0912-1, 2019.

693 Sadavarte, P., Pandey, S., Maasakkers, J. D., Lorente, A., Borsdorff, T., Denier van der Gon, H., Houweling, S. and Aben, I.:
694 Methane Emissions from Superemitting Coal Mines in Australia Quantified Using TROPOMI Satellite Observations,
695 *Environ. Sci. Technol.*, 55(24), 16573–16580, doi:10.1021/acs.est.1c03976, 2021.

696 Sánchez-García, E., Gorroño, J., Irakulis-Loitxate, I., Varon, D. J. and Guanter, L.: Mapping methane plumes at very high
697 spatial resolution with the WorldView-3 satellite, *Atmos. Meas. Tech. Discuss.*, 2021, 1–26, doi:10.5194/amt-2021-238,
698 2021.

699 Saunois, M., Bousquet, P., Poulter, B., Peregon, A., Ciais, P., Canadell, J. G., Dlugokencky, E. J., Etiope, G., Bastviken, D.,
700 Houweling, S., Janssens-Maenhout, G., Tubiello, F. N., Castaldi, S., Jackson, R. B., Alexe, M., Arora, V. K., Beerling, D. J.,
701 Bergamaschi, P., Blake, D. R., Brailsford, G., Brovkin, V., Bruhwiler, L., Crevoisier, C., Crill, P., Covey, K., Curry, C.,
702 Frankenberg, C., Gedney, N., Höglund-Isaksson, L., Ishizawa, M., Ito, A., Joos, F., Kim, H.-S., Kleinen, T., Krummel, P.,
703 Lamarque, J.-F., Langenfelds, R., Locatelli, R., Machida, T., Maksyutov, S., McDonald, K. C., Marshall, J., Melton, J. R.,
704 Morino, I., Naik, V., O'Doherty, S., Parmentier, F.-J. W., Patra, P. K., Peng, C., Peng, S., Peters, G. P., Pison, I., Prigent, C.,
705 Prinn, R., Ramonet, M., Riley, W. J., Saito, M., Santini, M., Schroeder, R., Simpson, I. J., Spahni, R., Steele, P., Takizawa,
706 A., Thornton, B. F., Tian, H., Tohjima, Y., Viovy, N., Voulgarakis, A., van Weele, M., van der Werf, G. R., Weiss, R.,
707 Wiedinmyer, C., Wilton, D. J., Wiltshire, A., Worthy, D., Wunch, D., Xu, X., Yoshida, Y., Zhang, B., Zhang, Z. and Zhu,
708 Q.: The global methane budget 2000–2012, *Earth Syst. Sci. Data*, 8(2), 697–751, doi:10.5194/essd-8-697-2016, 2016.

709 Saunois, M., Stavert, A. R., Poulter, B., Bousquet, P., Canadell, J. G., Jackson, R. B., Raymond, P. A., Dlugokencky, E. J.,
710 Houweling, S., Patra, P. K., Ciais, P., Arora, V. K., Bastviken, D., Bergamaschi, P., Blake, D. R., Brailsford, G., Bruhwiler,
711 L., Carlson, K. M., Carroll, M., Castaldi, S., Chandra, N., Crevoisier, C., Crill, P. M., Covey, K., Curry, C. L., Etiope, G.,
712 Frankenberg, C., Gedney, N., Hegglin, M. I., Höglund-Isaksson, L., Hugelius, G., Ishizawa, M., Ito, A., Janssens-Maenhout,
713 G., Jensen, K. M., Joos, F., Kleinen, T., Krummel, P. B., Langenfelds, R. L., Laruelle, G. G., Liu, L., Machida, T.,
714 Maksyutov, S., McDonald, K. C., McNorton, J., Miller, P. A., Melton, J. R., Morino, I., Müller, J., Murguia-Flores, F., Naik,
715 V., Niwa, Y., Noce, S., O'Doherty, S., Parker, R. J., Peng, C., Peng, S., Peters, G. P., Prigent, C., Prinn, R., Ramonet, M.,
716 Regnier, P., Riley, W. J., Rosentreter, J. A., Segers, A., Simpson, I. J., Shi, H., Smith, S. J., Steele, L. P., Thornton, B. F.,

717 Tian, H., Tohjima, Y., Tubiello, F. N., Tsuruta, A., Viovy, N., Voulgarakis, A., Weber, T. S., van Weele, M., van der Werf,
718 G. R., Weiss, R. F., Worthy, D., Wunch, D., Yin, Y., Yoshida, Y., Zhang, W., Zhang, Z., Zhao, Y., Zheng, B., Zhu, Q., Zhu,
719 Q. and Zhuang, Q.: The Global Methane Budget 2000–2017, *Earth Syst. Sci. Data*, 12(3), 1561–1623, doi:10.5194/essd-12-
720 1561-2020, 2020.

721 Schellnhuber, H. J., Rahmstorf, S. and Winkelmann, R.: Why the right climate target was agreed in Paris, *Nat. Clim. Chang.*,
722 6(7), 649–653, doi:10.1038/nclimate3013, 2016.

723 Schurer, A. P., Cowtan, K., Hawkins, E., Mann, M. E., Scott, V. and Tett, S. F. B.: Interpretations of the Paris climate target,
724 *Nat. Geosci.*, 11(4), 220–221, doi:10.1038/s41561-018-0086-8, 2018.

725 Sha, M. K., Langerock, B., Blavier, J.-F. L., Blumenstock, T., Borsdorff, T., Buschmann, M., Dehn, A., De Mazière, M.,
726 Deutscher, N. M., Feist, D. G., García, O. E., Griffith, D. W. T., Grutter, M., Hannigan, J. W., Hase, F., Heikkinen, P.,
727 Hermans, C., Iraci, L. T., Jeseck, P., Jones, N., Kivi, R., Kumps, N., Landgraf, J., Lorente, A., Mahieu, E., Makarova, M. V.,
728 Mellqvist, J., Metzger, J.-M., Morino, I., Nagahama, T., Notholt, J., Ohyama, H., Ortega, I., Palm, M., Petri, C., Pollard, D.
729 F., Rettinger, M., Robinson, J., Roche, S., Roehl, C. M., Röhling, A. N., Rousogenous, C., Schneider, M., Shiomi, K., Smale,
730 D., Stremme, W., Strong, K., Sussmann, R., Té, Y., Uchino, O., Velazco, V. A., Vigouroux, C., Vrekoussis, M., Wang, P.,
731 Warneke, T., Wizenberg, T., Wunch, D., Yamanouchi, S., Yang, Y. and Zhou, M.: Validation of methane and carbon
732 monoxide from Sentinel-5 Precursor using TCCON and NDACC-IRWG stations, *Atmos. Meas. Tech.*, 14(9), 6249–6304,
733 doi:10.5194/amt-14-6249-2021, 2021.

734 Shoemaker, J. K., Schrag, D. P., Molina, M. J. and Ramanathan, V.: What role for short-lived climate pollutants in
735 mitigation policy?, *Science* (80- .), 342(6164), 1323–1324, 2013.

736 Smith, M. L., Gvakharia, A., Kort, E. A., Sweeney, C., Conley, S. A., Faloona, I., Newberger, T., Schnell, R., Schwietzke, S.
737 and Wolter, S.: Airborne Quantification of Methane Emissions over the Four Corners Region, *Environ. Sci. Technol.*,
738 51(10), 5832–5837, doi:10.1021/acs.est.6b06107, 2017.

739 Subramanian, R., Williams, L. L., Vaughn, T. L., Zimmerle, D., Roscioli, J. R., Herndon, S. C., Yacovitch, T. I.,
740 Floerchinger, C., Tkacik, D. S., Mitchell, A. L., Sullivan, M. R., Dallmann, T. R. and Robinson, A. L.: Methane Emissions
741 from Natural Gas Compressor Stations in the Transmission and Storage Sector: Measurements and Comparisons with the
742 EPA Greenhouse Gas Reporting Program Protocol, *Environ. Sci. Technol.*, 49(5), 3252–3261, doi:10.1021/es5060258, 2015.

743 Suto, H., Kataoka, F., Kikuchi, N., Knuteson, R. O., Butz, A., Haun, M., Buijs, H., Shiomi, K., Imai, H. and Kuze, A.:
744 Thermal and near-infrared sensor for carbon observation Fourier transform spectrometer-2 (TANSO-FTS-2) on the
745 Greenhouse gases Observing SATellite-2 (GOSAT-2) during its first year in orbit, *Atmos. Meas. Tech.*, 14(3), 2013–2039,
746 doi:10.5194/amt-14-2013-2021, 2021.

747 The European Union’s Copernicus Climate Change Service: Annual summary 2021. [online] Available from:
748 https://climate.copernicus.eu/sites/default/files/custom-uploads/Annual_summary_2021/C3S-CAMS annual temp data and CO2 2021_press release_final.pdf, n.d.

750 Thompson, D. R., Thorpe, A. K., Frankenberg, C., Green, R. O., Duren, R., Guanter, L., Hollstein, A., Middleton, E., Ong,
751 L. and Ungar, S.: Space-based remote imaging spectroscopy of the Aliso Canyon CH₄ superemitter, *Geophys. Res. Lett.*,
752 43(12), 6571–6578, doi:<https://doi.org/10.1002/2016GL069079>, 2016.

753 Thorpe, A. K., Frankenberg, C., Aubrey, A. D., Roberts, D. A., Nottrott, A. A., Rahn, T. A., Sauer, J. A., Dubey, M. K.,
754 Costigan, K. R., Arata, C., Steffke, A. M., Hills, S., Haselwimmer, C., Charlesworth, D., Funk, C. C., Green, R. O.,
755 Lundein, S. R., Boardman, J. W., Eastwood, M. L., Sarture, C. M., Nolte, S. H., Mccubbin, I. B., Thompson, D. R. and
756 McFadden, J. P.: Mapping methane concentrations from a controlled release experiment using the next generation airborne
757 visible/infrared imaging spectrometer (AVIRIS-NG), *Remote Sens. Environ.*, 179, 104–115,
758 doi:<https://doi.org/10.1016/j.rse.2016.03.032>, 2016.

759 Tuzson, B., Graf, M., Ravelid, J., Scheidegger, P., Kupferschmid, A., Looser, H., Morales, R. P. and Emmenegger, L.: A
760 compact QCL spectrometer for mobile, high-precision methane sensing aboard drones, *Atmos. Meas. Tech.*, 13(9), 4715–
761 4726, doi:10.5194/amt-13-4715-2020, 2020.

762 United Nations: Global methane pledge, [online] Available from: <https://unfccc.int/news/world-leaders-kick-start-accelerated-climate-action-at-cop26>, 2021.

763 Varon, D., McKeever, J., Jervis, D., Maasakkers, J. D., Pandey, S., Houweling, S., Aben, I., Scarpelli, T. and Jacob, D. J.:
764 Satellite Discovery of Anomalously Large Methane Point Sources From Oil/Gas Production, *Geophys. Res. Lett.*, 46,
765 doi:10.1029/2019GL083798, 2019.

766 Varon, D. J., Jacob, D. J., McKeever, J., Jervis, D., Durak, B. O. A., Xia, Y. and Huang, Y.: Quantifying methane point
767 sources from fine-scale satellite observations of atmospheric methane plumes, *Atmos. Meas. Tech.*, 11(10), 5673–5686,
768 doi:10.5194/amt-11-5673-2018, 2018.

769 Varon, D. J., Jacob, D. J., Jervis, D. and McKeever, J.: Quantifying Time-Averaged Methane Emissions from Individual
770 Coal Mine Vents with GHGSat-D Satellite Observations, *Environ. Sci. Technol.*, 54(16), 10246–10253,
771 doi:10.1021/acs.est.0c01213, 2020.

772 Varon, D. J., Jervis, D., McKeever, J., Spence, I., Gains, D. and Jacob, D. J.: High-frequency monitoring of anomalous
773 methane point sources with multispectral Sentinel-2 satellite observations, *Atmos. Meas. Tech.*, 14(4), 2771–2785,
774 doi:10.5194/amt-14-2771-2021, 2021.

775 Vaughn, T. L., Bell, C. S., Pickering, C. K., Schwietzke, S., Heath, G. A., Pétron, G., Zimmerle, D. J., Schnell, R. C. and
776 Nummedal, D.: Temporal variability largely explains top-down/bottom-up difference in methane emission estimates from a
777 natural gas production region, *Proc. Natl. Acad. Sci.*, 115(46), 11712–11717, 2018.

778 Veefkind, J. P., Aben, I., McMullan, K., Förster, H., de Vries, J., Otter, G., Claas, J., Eskes, H. J., de Haan, J. F., Kleipool,
779 Q., van Weele, M., Hasekamp, O., Hoogeveen, R., Landgraf, J., Snel, R., Tol, P., Ingmann, P., Voors, R., Kruizinga, B.,
780 Vink, R., Visser, H. and Levelt, P. F.: TROPOMI on the ESA Sentinel-5 Precursor: A GMES mission for global
781 observations of the atmospheric composition for climate, air quality and ozone layer applications, *Remote Sens. Environ.*,
782 120, 70–83, doi:<https://doi.org/10.1016/j.rse.2011.09.027>, 2012.

784 Verhoelst, T., Compernolle, S., Pinardi, G., Lambert, J.-C., Eskes, H. J., Eichmann, K.-U., Fjæraa, A. M., Granville, J.,
785 Niemeijer, S., Cede, A., Tiefengraber, M., Hendrick, F., Pazmiño, A., Bais, A., Bazureau, A., Boersma, K. F., Bognar, K.,
786 Dehn, A., Donner, S., Elokhov, A., Gebetsberger, M., Goutail, F., Grutter de la Mora, M., Gruzdev, A., Gratsea, M., Hansen,
787 G. H., Irie, H., Jepsen, N., Kanaya, Y., Karagkiozidis, D., Kivi, R., Kreher, K., Levelt, P. F., Liu, C., Müller, M., Navarro
788 Comas, M., Piters, A. J. M., Pommereau, J.-P., Portafaix, T., Prados-Roman, C., Puentedura, O., Querel, R., Remmers, J.,
789 Richter, A., Rimmer, J., Rivera Cárdenas, C., Saavedra de Miguel, L., Sinyakov, V. P., Stremme, W., Strong, K., Van
790 Rozendaal, M., Veefkind, J. P., Wagner, T., Wittrock, F., Yela González, M. and Zehner, C.: Ground-based validation of
791 the Copernicus Sentinel-5P TROPOMI NO₂ measurements with the NDACC ZSL-DOAS, MAX-DOAS and Pandonia
792 global networks, *Atmos. Meas. Tech.*, 14(1), 481–510, doi:10.5194/amt-14-481-2021, 2021.
793 World Meteorological Organization: Global Atmosphere Watch Programme (GAW), [online] Available from:
794 <https://community.wmo.int/activity-areas/gaw>, 2022.
795 Yang, X., Ye, Y., Li, X., Lau, R. Y. K., Zhang, X. and Huang, X.: Hyperspectral Image Classification With Deep Learning
796 Models, *IEEE Trans. Geosci. Remote Sens.*, 56(9), 5408–5423, doi:10.1109/TGRS.2018.2815613, 2018.
797 Yu, S., Jia, S. and Xu, C.: Convolutional neural networks for hyperspectral image classification, *Neurocomputing*, 219, 88–
798 98, doi:<https://doi.org/10.1016/j.neucom.2016.09.010>, 2017.
799 Yuan, Q., Shen, H., Li, T., Li, Z., Li, S., Jiang, Y., Xu, H., Tan, W., Yang, Q., Wang, J., Gao, J. and Zhang, L.: Deep
800 learning in environmental remote sensing: Achievements and challenges, *Remote Sens. Environ.*, 241, 111716,
801 doi:<https://doi.org/10.1016/j.rse.2020.111716>, 2020.
802 Zavala-Araiza, D., Lyon, D., Alvarez, R. A., Palacios, V., Harriss, R., Lan, X., Talbot, R. and Hamburg, S. P.: Toward a
803 Functional Definition of Methane Super-Emitters: Application to Natural Gas Production Sites, *Environ. Sci. Technol.*,
804 49(13), 8167–8174, doi:10.1021/acs.est.5b00133, 2015.
805 Zavala-Araiza, D., Alvarez, R. A., Lyon, D. R., Allen, D. T., Marchese, A. J., Zimmerle, D. J. and Hamburg, S. P.: Super-
806 emitters in natural gas infrastructure are caused by abnormal process conditions, *Nat. Commun.*, 8(1), 14012,
807 doi:10.1038/ncomms14012, 2017.
808 Zhang, M., Li, W. and Du, Q.: Diverse Region-Based CNN for Hyperspectral Image Classification, *IEEE Trans. Image
809 Process.*, 27(6), 2623–2634, doi:10.1109/TIP.2018.2809606, 2018.
810
811